ORNL/TM-2017/250
CRADA/NFE-12-04273

Energy Efficient Clothes Dryer— Final Report

This document has been reviewed and is determined to be APPROVED FOR PUBLIC RELEASE.

Name/Title: Leesa Laymance/ORNL TIO
Date: 8/31/2020

Kyle R. Gluesenkamp
Bo Shen
Philip Boudreaux

May 2017

OFFICIAL USE ONLY
May be exempt [illegible]lic release under the Freedom [illegible]ation Act (5 U.S.C. 552), exe[illegible]umber and category: 4 [illegible]rcial/Proprietary
Department of Energy [illegible] required before pu[illegible]ase

Name/Org: Kyle Gluesenka[illegible]L Da[illegible]2017
Guidance (if applicable): N/A

PROTECTE[illegible]FORMATION

This product contains [illegible]ted CRA[illegible]formation which was produced on Septe[illegible], 2016 under [illegible] No. NFE-12-04273 and is not to be [illegible] disclosed for a perio[illegible]ree years from the date it wa[illegible]uced except as expressly p[illegible]d for in the CRADA.

OAK RIDGE NATIONAL LABORATORY
MANAGED BY UT-BATTELLE FOR THE US DEPARTMENT OF ENERGY

~~OFFICIAL USE ONLY~~

DOCUMENT AVAILABILITY

Reports produced after January 1, 1996, are generally available free via US Department of Energy (DOE) SciTech Connect.

Website http://www.osti.gov/scitech/

Reports produced before January 1, 1996, may be purchased by members of the public from the following source:

National Technical Information Service
5285 Port Royal Road
Springfield, VA 22161
Telephone 703-605-6000 (1-800-553-6847)
TDD 703-487-4639
Fax 703-605-6900
E-mail info@ntis.gov
Website http://classic.ntis.gov/

Reports are available to DOE employees, DOE contractors, Energy Technology Data Exchange representatives, and International Nuclear Information System representatives from the following source:

Office of Scientific and Technical Information
PO Box 62
Oak Ridge, TN 37831
Telephone 865-576-8401
Fax 865-576-5728
E-mail reports@osti.gov
Website http://www.osti.gov/contact.html

ORNL/TM-2017/250
CRADA/NFE-12-04273

Energy and Transportation Science Division

ENERGY EFFICIENT CLOTHES DRYER – FINAL REPORT

Kyle Gluesenkamp
Bo Shen
Philip Boudreaux

Date Published: May 2017

Prepared by
OAK RIDGE NATIONAL LABORATORY
Oak Ridge, TN 37831-6283
managed by
UT-BATTELLE, LLC
for the
US DEPARTMENT OF ENERGY
under contract DE-AC05-00OR22725

CONTENTS

LIST OF FIGURES

LIST OF TABLES

NOMENCLATURE

ΔP	pressure difference or pressure drop
BTO	Building Technologies Office
CEF	combined energy factor
CFM	cubic feet per minute
CFR	US Code of Federal Regulations
COP	coefficient of performance
D1	CFR appendix containing post-2015 test procedure for evaluating CEF
DOE	Department of Energy
EES	Engineering Equation Solver
EF	energy factor
EXV	electronic expansion valve
GEA	GE Appliances
HPCD	heat pump clothes dryer
HPDM	Heat Pump Design Model
HVAC	heating, ventilation, and air-conditioning
K	Kelvin
NI	National Instruments
Q	heat flow [kW or Btu/hr]
RH	relative humidity
RMC	remaining moisture content [mass of water per mass of dry cloth]
TP	test procedure
VC	vapor-compression

ABSTRACT AND STATEMENT OF OBJECTIVES

The purpose of this project was to conduct research and development to evaluate the technical and commercial viability of a residential heat pump clothes dryer that enables reduced energy consumption by utilizing waste heat from the clothes drying process. The clothes dryer design focused on developing a heat pump cycle that significantly reduces energy consumption compared to conventional resistance heaters. General Electric Appliances (GEA) is the world leader in appliances and has commercialized numerous appliance innovations for the US residential market.

Existing heat pump clothes dryers on the market have extremely small market share. To improve this, the project focused on reducing cost, reducing cycling time, and maintaining or improving energy efficiency.

The critical outcomes of this project are the development of a heat pump clothes dryer for the US residential market.

1. US RESIDENTIAL CLOTHES DRYERS BACKGROUND

In the United States, the majority of clothes dryers use electric resistance heaters with a capacity of approximately 4 kW for clothes drying. US dryers typically use a tumble-type drum with a blower to push air and dry clothes. Most existing electric products are electric resistance with once-through airflow, with some condensing dryers using closed-loop airflow. Starting in late 2014, vapor-compression (VC) heat pump dryers have been available. Although they are extensively used in Australia and Europe, they have very low market penetration in the United States. Currently a few heat pump clothes dryers (HPCD) using R134a are available on the market from LG, Whirlpool, and Asko, but they have very high retail prices and relatively long dry times. Two are closed loop, and one uses open-loop airflow. Table 1 provides a summary of the combined energy factor (CEF), drying time, and range of retail prices for existing conventional dryers and existing HPCD products, along with CEF and drying time for HPCD prototypes developed during this project. The major market barriers are seen as the high cost and longer dry times (Denkenberger et al. 2013).

Table 1. Performance and cost of existing clothes drying technologies compared with performance of the prototype HPCD developed under this project

Type	CEF	Dry time [minutes]	Retail [$US]
Electric resistance	3.7–4.0	20–40	300–1200
Hybrid heat pump	4.5–7	70–120	1400–1600
This project (HP only mode)	*7*	*58*	*TBD*
This project (hybrid mode)	*5.5*	*43*	*TBD*

2. BENEFITS TO BUILDING TECHNOLOGIES OFFICE'S MISSION

The Department of Energy's (DOE) Building Technologies Office (BTO) has as its long-term goal to create marketable technologies and design approaches that address energy consumption in existing and new buildings. The current vision that BTO has for achieving this goal involves reducing the energy use intensity (EUI) and carbon emissions used by the energy service equipment (equipment providing space heating and cooling, water heating, etc.) by 50% compared to today's best common practice. Designs using heat pumps for applications such as space conditioning and water heating have been proven to have the capability for significantly reducing energy. However, heat pumps have not been widely applied to laundry products in the United States.

The BTO Multi-Year Program Plan released in 2016 (Department of Energy 2016) has a goal of 6.0 CEF for clothes dryers by 2020.

3. TECHNICAL DISCUSSION OF WORK PERFORMED BY ALL PARTIES

A broad overview of the research under this CRADA, including experimental and modeling activities, is shown in Figure 1. The project involved extensive prototype design, fabrication, and evaluation, as well as extensive model development, validation, and optimization.

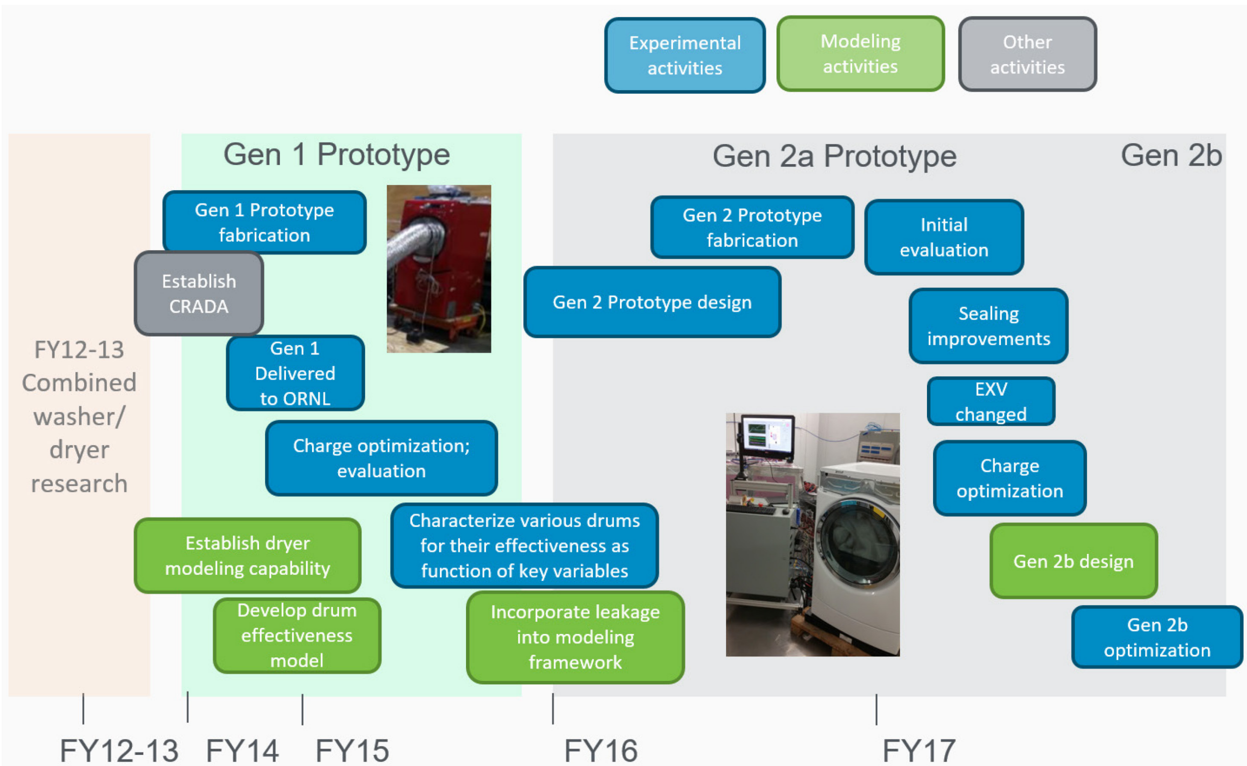

Figure 1. Broad overview and timeline of CRADA NFE-12-04273 research activities.

3.1 TEST FACILITY AND EXPERIMENTAL MEASUREMENT METHODOLOGY

The second generation HPCD was instrumented to monitor the changing state points of the air in the closed loop, the power consumption of all components, and the refrigerant temperature and pressure at critical locations. Figure 2 shows the location of all the sensors and the type of sensors installed on the prototype HPCD. Table 2 shows the sensor type, model, and uncertainty for all sensors that were used in the system.

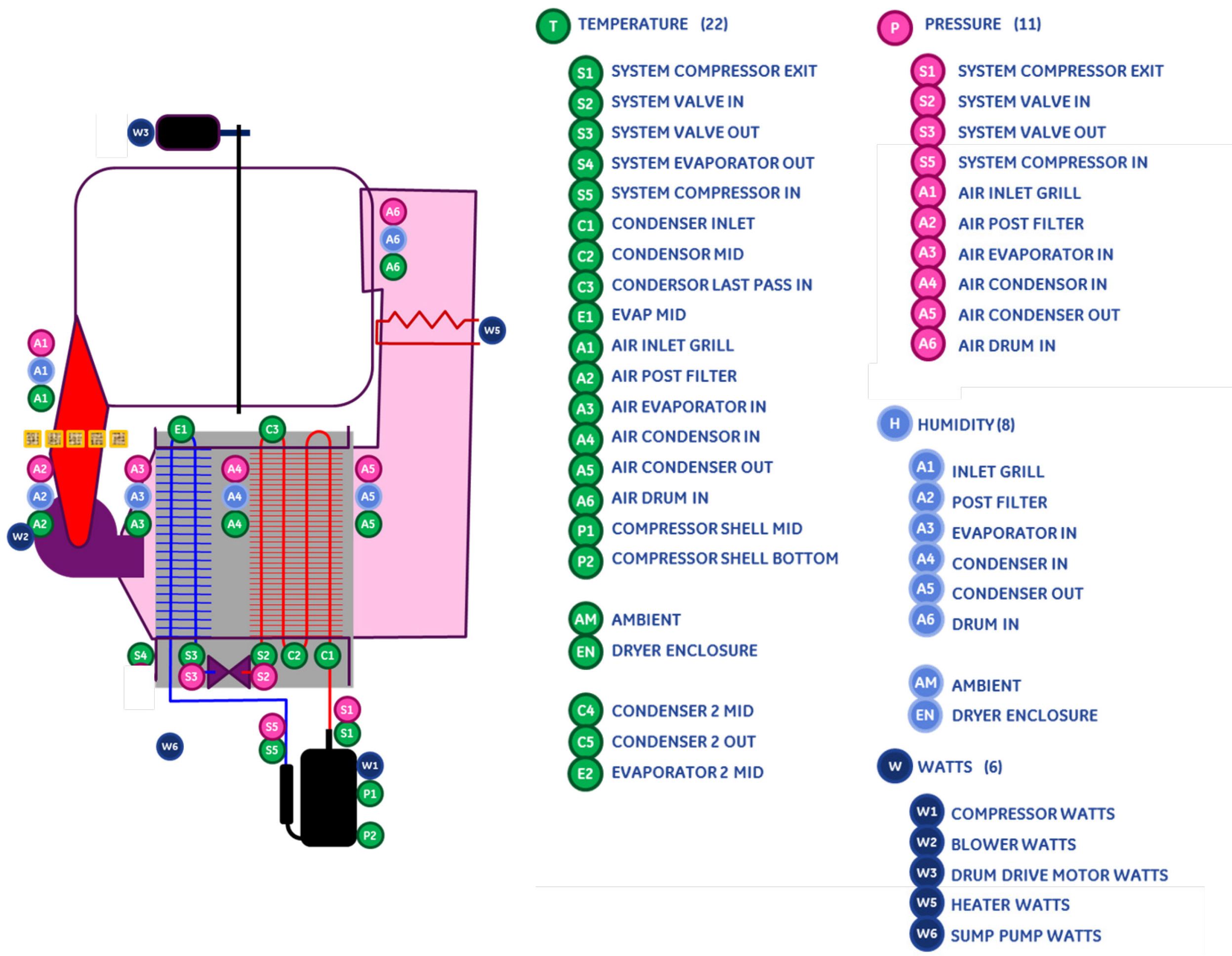

Figure 2. Schematic of second generation HPCD prototype with type and locations of all sensors.

Table 2. Type and accuracy of sensors used for lab test prototype HPCD

Measurement	Sensor Type	Uncertainty	Range/Full Scale
Temperature	Type T Thermocouples	±0.75% or ± 1.0 C whichever is greater	-454–700°F
Humidity	TE Connectivity HM1500LF	±2% @55%RH	0–100%
Air Pressure	Omega PX274	±1% Full Scale	±3.75 in. W.C.
Refrigerant Pressure	Omega PX409-500AI PX409-250AI	±0.08% Full Scale	0–500 PSIA (S1, S2) 0–250 PSIA (S3, S5)
Power	OSI GW5-014E GW5-121E GW5-019C	±0.04% Full Scale	0–4kW (W1, W5) 0–400W (W3) 0–2kW (W2)
Airflow	Air Monitor Corporation Veltron DPT-2500 with 4 in. Aluminum LO-flo Pitot Traverse Station	2% of actual flow	35–400 CFM

The efficiency (CEF) tests were completed per the standard testing protocol outlined in the Code of Federal Regulations (CFR) Pt. 430, Subpt. B, App. D1. The dryer was placed in a climate chamber, and the ambient temperature and relative humidity were controlled to 75±3°F and 50±10% relative humidity (RH), respectively.

To control the dryer operation and acquire data, LabVIEW virtual instruments were used with National Instruments (NI) data acquisition hardware. A NI CompactDAQ 8-slot data logger was used with the following data acquisition modules: NI-9213 for thermocouples, NI-9208 current input module for air and refrigerant pressure as well as power, and a NI-9205 voltage input module for humidity measurements. For control a NI-9481 relay output module was used for relay control of the compressor, heater, and drum rotation. Also a NI-9474 digital module was used to control the position of the electronic expansion valve (EXV) valve.

A custom LabVIEW virtual instrument was used to control the dryer through a dry cycle and collect data. Data was sampled at 20 kHz for current and voltage measurement and on demand for temperature measurements, and then every 6 seconds the average value for each channel was saved to disc. A feedback proportional-integral-derivative (PID) control loop was used for the automatic control of the EXV valve to maintain superheat at 8°F. Cycle termination was based on the difference between the drum inlet and exit mixing ratio: a measure of the absolute water content in the air. Once a difference of approximately 0.005 [kg of H_2O/kg dry air] was achieved, the cycle was terminated, which typically resulted in a 4% final moisture content of the 8.45 lb test load. Figure 3 shows the main tab of the LabVIEW virtual instrument used for HPCD control.

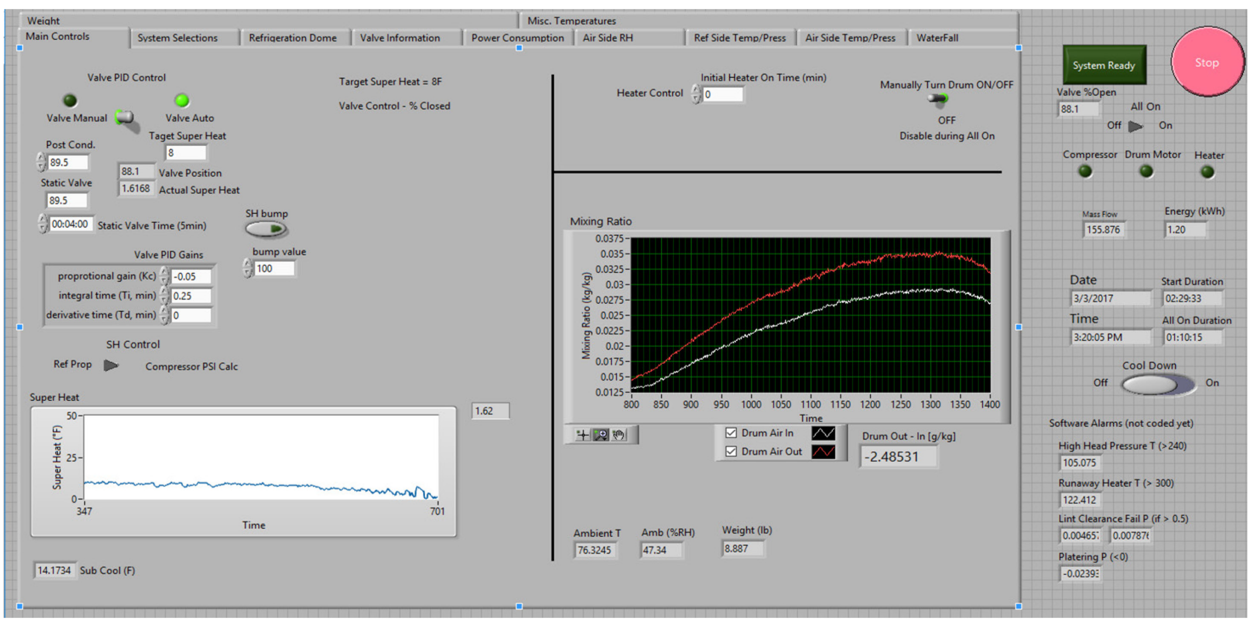

Figure 3. The main tab of the HPCD control program is used to monitor and control EXV position and superheat, as well as monitor the absolute moisture of the air coming into and out of the drum.

3.1.1 CEF Measurement

There are three fundamental energy-consuming components to a HPCD: the compressor, blower, and drum rotator. Typically, a single, dual-shafted motor drives both the blower and drum rotation.

For a production appliance, these three components are not separated; however, they were independently measured in the prototype. Furthermore, an outboard blower was used for many tests for ease of modulating the airflow rate. The methodology of how CEF was computed for each blower case is enumerated in Table 3.

Referring to Table 3, the simplest case is when the production blower was used: here the power measured by a Watt transducer was used directly for the dual-axis motor. The conversion of electrical energy into air movement had an efficiency of 17% with the production motor and blower (determined by subtracting the separately measured drum rotation torque and RPM).

When the EBM Papst outboard blower was used, the 120 VAC power into the fan controller was similarly measured directly by a Watt transducer. The blower efficiency was higher at 24%; however, it is important to note that the power consumed by the motor to rotate the drum barely decreased, despite being substantially unloaded. This actually results in a significant overestimation of the prototype power consumption by about 150 W.

When the McMaster outboard blower was used, the power was not measured directly. Instead, the cubic feet per minute (CFM) and pressure drop (ΔP) across the blower were measured, and a 24% electrical-to-flow work efficiency factor was applied.

Table 3. Methods used for computing CEF of dryer tests

	power consumption					CFR TP			
			fan power			ambient			
blower used	compr-essor power	drum power	fan power	ΔP used to calculate fan power	fan eff	T/RH	ΔRMC corr-ection	standby power (CEF)	4% penalty (DOE auto-term. corr. factor 1.04)
production	meas (AC)	meas[4] (~350 W)	meas[4] (AC)	N/A	17%	72-78°F/40-60%RH	yes	yes (calc[2])	yes
EBM Papst		meas[5] (~300 W)	meas (125 W)	N/A	24%				
McMaster		meas[5] (~300 W)	calc[1] (~185 W)	meas	24%[1]				
McMaster - theoretical		calc[3] (~150 W)	calc[1]	meas	24%[1]				

footnotes:

1. using $W_{flow,theoretical}$ = VFR*DP, and assuming $W_{flow,theoretical} / W_{electrical} = 0.24$
2. use typical value for best in class commercialized systems: 0.08 $W_{standby}$
   (0.2% CEF effect, or 8665 hrs/yr @ 283 cycles/yr = 2.45 Wh/cycle)
3. based on 90 W shaft power and assumed 0.60 motor efficiency
4. drum power and fan power were provided by a single motor
5. drum power remained high due to poor match between high torque motor and low torque load

Since most prototype results shown in this report are using one of the outboard blowers, where the drum rotation was consuming about 150 W more power than expected for a production system, the typical measurements reported in this report underestimate the CEF (as defined in CFR Appendix D1) by about 1 CEF point. A summary of differences between different test methods is provided in Gluesenkamp (2014).

3.2 FIRST GENERATION PROTOTYPE

The first generation prototype had the blower positioned between the condenser and drum, resulting in a positively pressurized drum, as was shown in Figure 2.

The HPCD was experimentally evaluated for a range of performance parameters, including refrigerant charge, blower volumetric flow rate, and auxiliary heater usage.

Gauge pressures were measured during dryer operation, as shown in Figure 4.

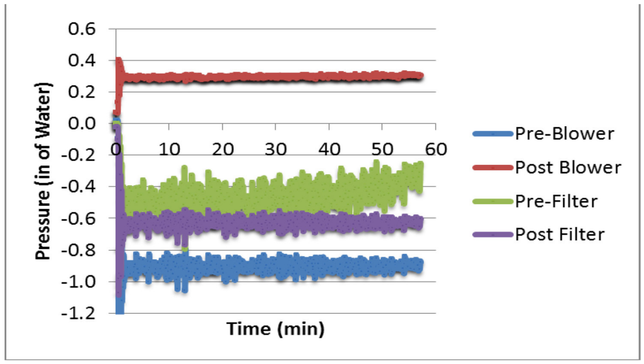

Figure 4. Gauge pressures of the first generation prototype during operation.

The clothing weight during the dry cycle was measured by a whole-dryer scale, and the remaining moisture content (RMC) was calculated as shown in Figure 5. The drainage pump pumps the accumulated water off of the scale every 5 minutes, leading to a staggered profile of the weight over time.

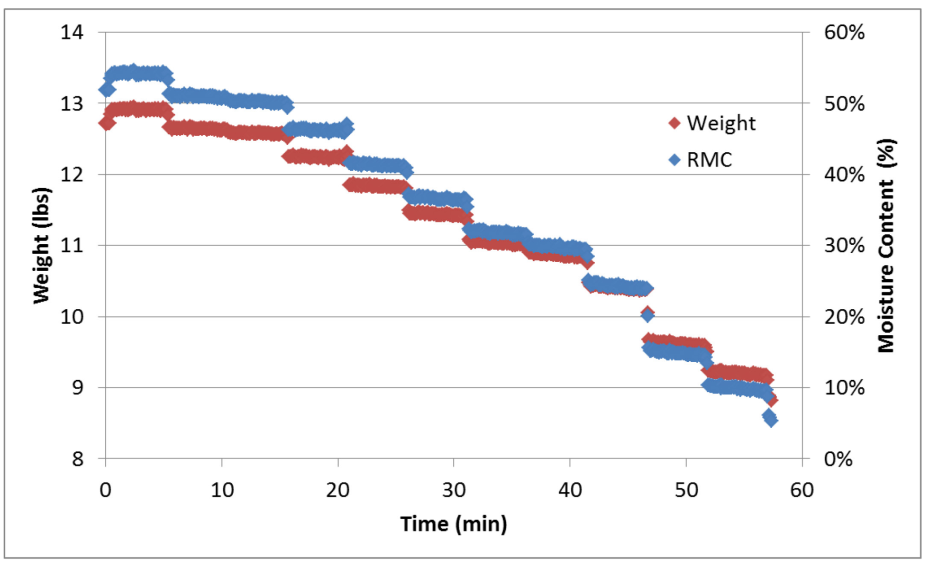

Figure 5. Load weight and RMC over time for the first generation prototype.

The power input to the cycle included power for the compressor, drum rotation, blower, and drain pump, as shown in Figure 6.

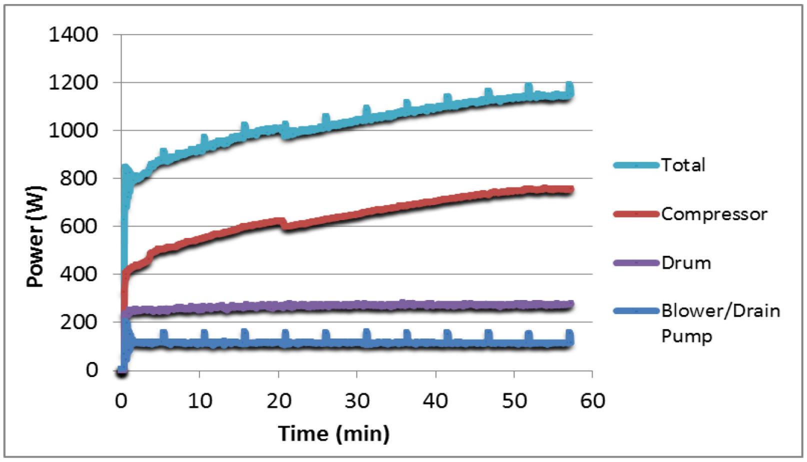

Figure 6. Power consumption of the first generation dryer over time.

Selected results for the first generation prototype are summarized in Table 4.

Table 4. First generation prototype Appendix D1 results

Test No.	Normalized Air Volumetric Flow Rate (CFM)	Corrected Dryer Time (min)	Initial Wet Weight (lb)	Moisture Removed (lb)	Energy Consumption (kWh)	Final Moisture Content	Corrected Energy Factor	Efficiency	Coefficient of Performance
1	Optimum (0.8)	56.30	13.37	4.61	1.00	2.87%	8.29	1.31	5.996
2	Optimum (0.8)	56.08	13.45	4.69	1.02	3.44%	8.26	1.31	5.305
3	Optimum (0.8)	56.17	13.36	4.60	0.99	3.38%	8.35	1.32	6.957
4	Optimum (0.8)	57.19	13.203	4.469	0.99	4.24%	8.11	1.28	5.963
5	0.7	59.80	12.92	4.28	1.00	3.16%	7.68	1.22	6.696
6	0.7	58.80	13.126	4.345	0.98	4.82%	7.97	1.26	6.371
7	0.9	56.33	13.49	4.78	1.04	3.73%	8.26	1.31	6.705
8	0.9	57.98	13.146	4.405	0.99	4.40%	8.00	1.26	7.298
9	1.0	60.18	12.92	4.24	0.99	3.61%	7.70	1.22	7.963
10	1.0	59.78	13.098	4.35	1.00	4.39%	7.82	1.24	8.001

In addition, the first generation prototype was run back to back over four tests to ensure it would not overheat, as shown in Figure 7. These four tests were run according to the Appendix D1 procedure.

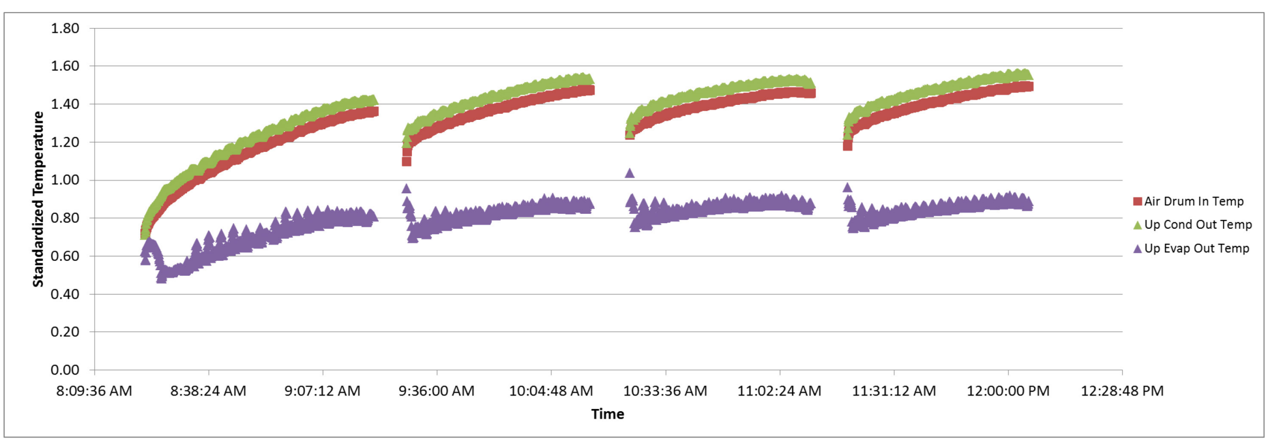

Figure 7. Temperatures for four back-to-back cycles of first generation prototype.

3.3 SECOND GENERATION PROTOTYPE

At the beginning of FY 2016, GE began designing the second generation prototype based on the cabinet and internals of the next generation of commercially available GE traditional dryer. This returned the design back to a negatively pressured drum (blower between drum and evaporator). Utilizing the existing platform required the incorporation of a refrigeration system and closed air loop within the existing cabinet. The stock motor that turned the drum and fan was used, and custom ducting was built to bring the air from the blower into the evaporator and condenser and then into the supplemental resistance heater and back into the rear of the drum.

Fabrication was complete during Q4 of FY 2016, and GE delivered the unit to ORNL. Upon delivery some hardware still required work such as installing sensors, air sealing, and fabricating some duct transitions. The software also needed to be written to control this new prototype. For this the NI LabVIEW virtual instrument from the first generation prototype was modified.

Once this work was done, shakedown testing began at the end of Q4 in FY 2016. This shakedown testing included reducing the initial R134a refrigerant charge from 16 oz down to 9.5 oz to keep the compressor from overheating. This exercise revealed that the EXV was undersized, at which point a larger EXV was installed.

After the new EXV was installed, a matrix of tests was completed to optimize charge, heater-on time, and super heat. For tests with the heater enabled, the electric resistance (1580 W) heater was turned on for 10 minutes at the start of the cycle. Table 5 shows the results for all tests in the matrix with CEF (using the EBM Pabst approach from Table 3) and cycle run time. It should be noted that a sequential approach was taken: in the first stage, refrigerant charge was optimized at a roughly constant airflow rate; later air flow was explored at that fixed refrigerant charge.

Table 5. Matrix results for optimizing charge, superheat and heater on time

Test	R134a Refrigerant Charge (oz)	Heater duration (min)	Target Superheat (°F)	Air flow rate (CFM)	CEF	Cycle Run Time (min)	Final Moisture Content (%RMC)
1	9.5	0	8	155	6.415	71.4	1.25
2	9.5	0	20	156	6.359	72.7	1.10
3	9.5	10	8	155	5.708	62.7	1.25
4	9.5	10	20	156	5.851	62.1	1.38
5	9.75	0	8	162	5.864	72.9	1.54
6	9.75	0	20	164	5.894	74.3	1.90
7	9.75	10	8	163	5.280	64.1	1.64
8	9.75	10	20	147	5.378	64.2	1.75
9	9	0	8	151	6.101	71.1	1.64
10	9	0	20	154	6.053	74.6	1.38
11	9	10	8	152	5.550	63.2	1.54
12	9	10	20	155	5.591	61.9	1.83

Figure 8 shows the results from Table 5 in graphical form. The number below the circle indicates the time the heater was on for the beginning of the cycle. Notice that having the heater on for 10 minutes reduces the cycle time by about the same amount.

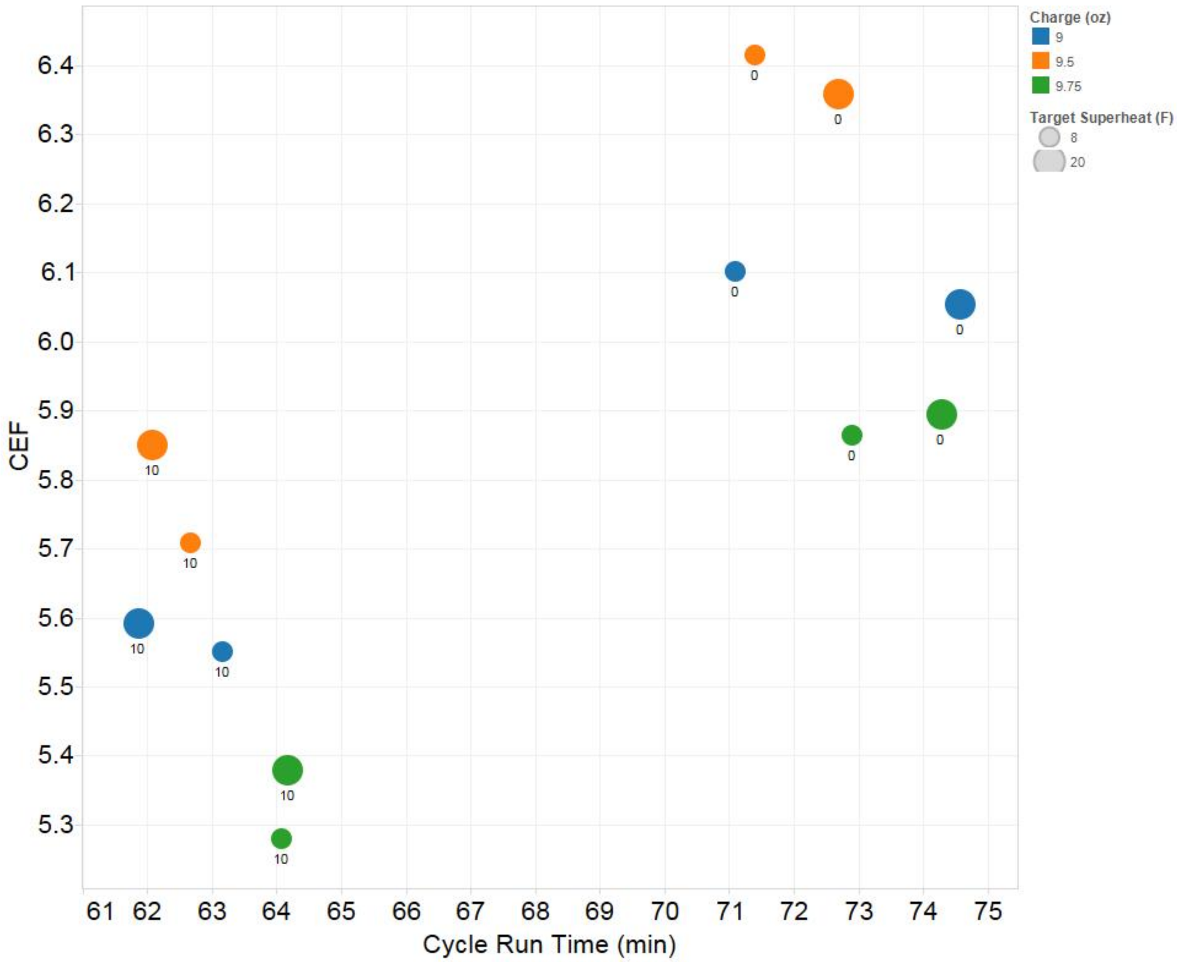

Figure 8. Graphical representation of test matrix results for optimizing charge, superheat and heater on time.

A charge of 9.5 oz results in the best CEF. The change in evaporator exit superheat affects the efficiency differently depending on whether the heater is used or not. When the heater is used for 10 minutes, the 8°F superheat results in lower CEFs and usually slower dry times. When no heater is used, the 8°F superheat usually results in quicker drying and higher CEF. On balance, the superheat is a very minor effect, and the refrigerant charge is much more important. Based on these results, a 9.5 oz charge was used with 8°F superheat for the remainder of the tests.

The next matrix (shown in Table 6) involved optimizing the airflow through the closed air loop of the dryer.

Two different blowers were used to test a range of flow rates. The EBM Papst blower was used which can be adjusted to enable different flow rates. The McMaster blower was also used, which provides a higher flow rate than the EBM Papst blower. Figure 9 shows the results of this matrix. The McMaster blower provided 174 CFM at about 2.2 in. water column static pressure difference (in. W.C.) during a CEF test. The EBM Pabst blower was used to provide 167 CFM at 1.45 in. W.C. and 134 CFM at 0.9 in. W.C. Notice that the higher flow rate yields higher CEF and faster dry times. To compute CEF, the EBP Papst method and McMaster method outlined in Table 3 were used for the respective blowers to find CEF.

Table 6. Matrix results for optimizing air flow rate

Test	R134a Refrigerant Charge (oz)	Heater duration (min)	Target Superheat (°F)	Air flow rate (CFM)	CEF	Cycle Run Time (min)	Final Moisture Content (%RMC)
1	9.5	0	8	156	6.325	67.47	3.34
2	9.5	0	8	162	6.178	70.67	2.56
3	9.5	0	8	144	6.217	67.87	4.44
4	9.5	0	8	175	5.970	70.38	1.83
5	9.5	0	8	174	6.690	59.88	4.44
6	9.5	0	8	174	6.675	59.37	4.44
7	9.5	0	8	167	6.311	70.28	2.20
8	9.5	0	8	134	6.064	75.50	1.62

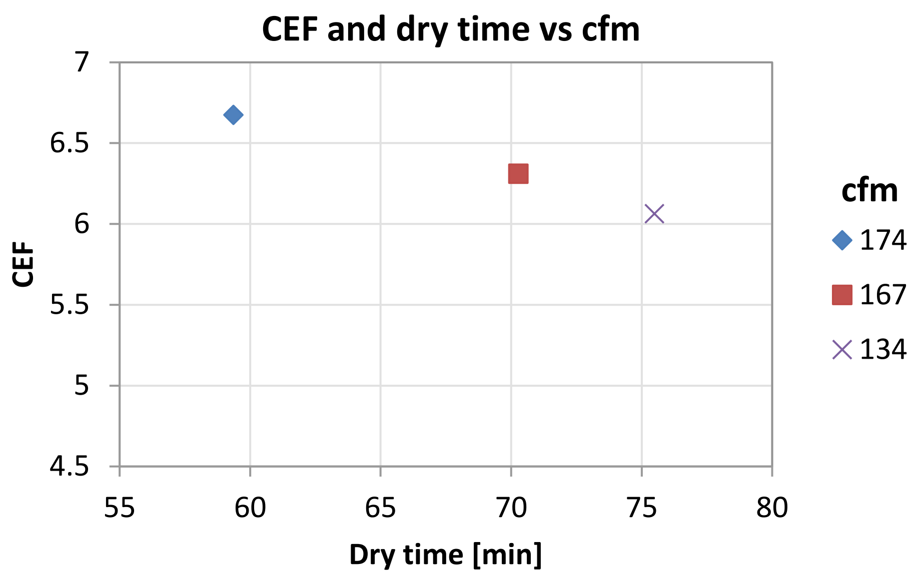

Figure 9. CEF and dry time results from different airflow rates.

3.4 LEAKAGE CHARACTERIZATION

3.4.1 Methodology

Understanding the location, magnitude, and direction of air leakage of the heat pump clothes dryer is critical for accurately characterizing the performance and developing a high-performance design. Three pieces of information are needed to understand the leakage characteristics of the closed air loop on the heat pump clothes dryer: (1) leakage characteristics of each segment along the airflow path, (2) the typical pressure drops across components in the airflow path (filter, evaporator, etc.); and (3) using the preceding information find the volumetric flow rate into or out of the airflow path at leakage locations. Each of these three components are discussed below followed by results from the second generation prototype.

3.4.1.1 Measuring leakage amount and locations - C_v

A Minneapolis Duct Blaster, typically used for measuring the leakage area of air-conditioning ducts in residential homes, is used to access the leakage amount and locations along the airflow path of the HPCD. The Duct Blaster operates by pressurizing the closed air loop of the HPCD to a range of pressures in reference to ambient. At each pressure the pressure difference across the fan is measured and converted to a volumetric flow rate (CFM) using the Duct Blaster fan curve. This flow rate is equal to the air moving out of the cracks and holes in the closed air loop at that particular air loop pressure. Once this is completed for multiple air loop pressures, the points of CFM vs pressure are fit to a power function shown in Eq. 1 that describes the flow through an orifice, where Q [CFM] is the flow rate at pressure p [Pa], C is the flow coefficient, and n is the flow exponent. C and n are used to describe the amount of leakage and can be used to compute a leakage area.

$$Q = Cp^n \,. \qquad \text{Eq. 1}$$

For our purposes we convert C to C_v, which is calculated by setting n = 0.5 and converting p from Pascals to inches of water and then fitting the data by varying C_v to get a good fit. This is useful in comparing the leakage characteristics at different locations in the air loop. A larger C_v at one location relative to another means there is a bigger hole in that location. If using C_v, then Eq. 1 becomes Eq. 2.

$$Q = C_v p^{0.5} \,. \qquad \text{Eq. 2}$$

To connect the Duct Blaster to the second generation dryer, a custom duct was made for connection of the fan between the electric heater and drum entrance (Figure 10). By utilizing this setup and taping off sections of the dryer air loop, the localized leakage characteristics could be evaluated.

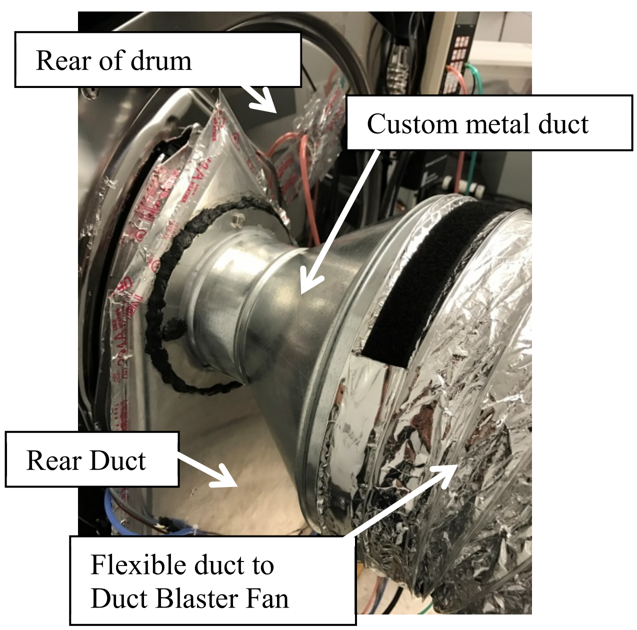

Figure 10. Custom metal duct to interface Duct Blaster to HPCD for leakage testing.

Figure 11 shows a schematic of the dryer air loop with the leakage locations (C_v) between the numbered components in the airflow path that can change the state of the air in the loop. There are eight distinct C_vs that can be measured. Due to the nature of the closed air path, C_vs could not be measured directly by completely isolating the component and instead had to be measured by subtracting one test from another with the component leakage under question taped and sealed completely. Other C_vs had to be computed using engineering judgment since they could not be isolated by subtraction (see C_v7 and C_v8).

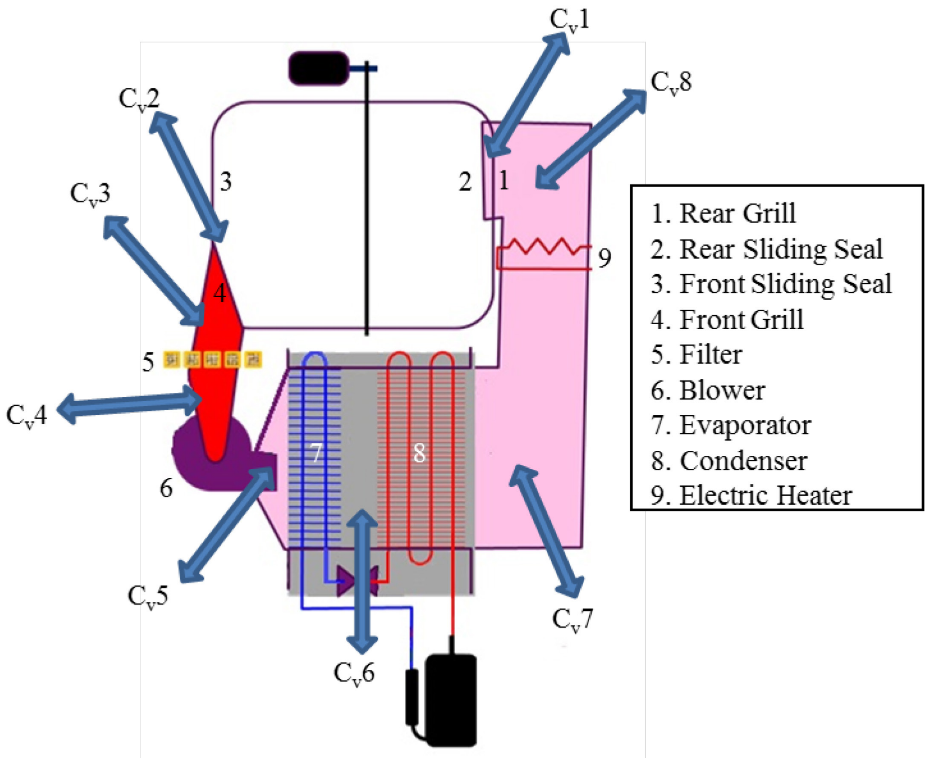

Figure 11. Schematic of HPCD air loop showing air leakage locations as $C_v\#$ and components that can produce pressure drops in airflow path.

Nine whole-dryer trials were conducted, each with a unique set of components taped off. Each trial resulted in a whole-dryer C_v value, which are denoted with arbitrary trial numbers (C_{vT1}, C_{vT2}, etc.) as described in the list below. Table 7 shows how these 9 trial results were used to determine the 8 C_v values of Figure 11 that are needed in the dryer analysis.

Cv_{T1}: Dryer in as-usual experimental state

$Cv_{T2:}$ Front sliding seal taped

$Cv_{T3:}$ Front and rear sliding seal taped

$Cv_{T4:}$ Front and rear sliding seal taped and duct between blower and filter removed

$Cv_{T5:}$ Front and rear sliding seal taped, duct between blower and filter removed, front grill taped and sealed

$Cv_{T6:}$ Front and rear sliding seal taped, duct between blower and filter removed, front grill taped and sealed, removed duct from blower to evaporator

$Cv_{T7:}$ Front and rear sliding seal taped, duct between blower and filter removed, front grill taped and sealed, removed duct from blower to evaporator, taped rear grill

$Cv_{T8:}$ Only rear duct from condenser outlet to rear grill (includes C_v7 and C_v8)

$Cv_{T9:}$ Rear duct plus condenser and evaporator with condenser outlet to rear duct transition taped and sealed

Table 7. Equations for computing C_vs based on trials listed above and measured results

C_v from Figure 11	Equation	Measured Results (second generation with outboard blower)
C_v1 (rear sliding seal)	$C_v1 = C_{vT2} - C_{vT3}$	18.2
C_v2 (front sliding seal)	$C_v2 = C_{vT1} - C_{vT2}$	17.7
C_v3 (front grill to filter)	$C_v3 = C_{vT4} - C_{vT5}$	4.0
C_v4 (filter to blower)	$C_v4 = C_{vT3} - C_{vT4}$	6.0
C_v5 (blower to evaporator)	$C_v5 = C_{vT5} - C_{vT6}$	0
C_v6 (evaporator to condenser)	$C_v6 = C_{vT9} - C_{vT8}$	13.8
C_v7 (condenser to heater)	$C_v7 = C_{vT7} - C_{vT9} + 0.5 * C_{vT8}$	15.7
C_v8 (heater to rear grill)	$C_v8 = C_{vT6} - C_{vT7} + 0.5 * C_{vT8}$	33.0

The results in Table 7 are with a static (i.e. non-rotating) drum. However, earlier studies on the first generation prototype showed that leakage can change up to 30% depending on the static position of the drum (Bansal 2016), due to the fact that the drum is not perfectly circular. The second generation prototype had much better sealing, and the variability was expected to be much less. For the second generation prototype, the difference in leakage during dynamic rotation (without any blower operation) versus at a single static position was measured. Table 8 describes these results, which show that a rotating drum increased the total dryer leakage by about 8%, representing about an 18% increase in the drum Cv value. Due to the small influence on the overall leakage calculation, the distinction between dynamic and static values was neglected, and the static values shown in Table 7 were used throughout the analysis described in this report.

Table 8. Comparison of total dryer leakage with static and rotating drum

	C_v [CFM/√inWC]
Total Dryer Leakage – Static Drum (1 position)	104.8
Total Dryer Leakage – Rotating Drum	113.5

3.4.1.2 Pressure drops across components in the airflow path

After the C_vs were measured, the pressure drops across seven components in the airflow path (evaporator, condenser, heater, rear grill, drum, front grill and filter) shown in Figure 11 needed to be found. The differential pressure at six locations was measured continuously during every dryer test: inlet grill, post filter, evaporator in, condenser in, condenser out, and drum, as shown in Figure 2. Similar to the C_v determination, some of the pressure drops can be computed by subtraction of the measured differential pressure measurements with respect to ambient, and other pressure drops required special experimentation. The pressure drops that were directly measured are across the evaporator, condenser, heater, and lint filter.

Referencing Figure 2, the following equations in Table 9 can be used to find the following pressure drops.

Table 9 Equations for determining pressure drops across components in air path loop

Pressure drop across component (ref. Figure 11)	Equation (ref. Figure 2)
7–Evaporator	A3-A4
8–Condenser	A4-A5
9–Heater	A5-A6
5–Lint Filter (clean)	A1-A2

To determine the pressure drop across the rear grill, drum, and front grill, an experiment was conducted where the differential pressure with respect to ambient was measured at the back of the drum and the front of the drum under different scenarios: tumble and airflow without clothes, with dry clothes, and with wet clothes. The pressure drops that were measured and calculated for each component for each scenario are shown in Table 10. These were conducted with a clean filter.

Table 10. Pressure drops across components that were not measured directly during normal energy factor (EF) testing of the HPCD

Component (ref. Figure 11)	No clothes with tumble – 192 CFM [in W.C.]	Dry clothes (8.45 lb, 2% MC) with tumble – 184 CFM [in W.C.]	Wet clothes (8.45 lb, 42% MC) with tumble – 184 CFM [in W.C.]
1–Rear Grill	0.004	0.021	0.012
2,3–Drum	0.089	0.082	0.093
4–Front Grill	0.036	0.542	0.562
5–Filter	0.85	0.682	0.658

3.4.1.3 Volumetric flow rate at leakage locations

Finally to compute the volumetric flow rate of leakage into and out of the clothes dryer airflow path, a custom-built simultaneous equation solver was developed that takes the C_v and pressure drops as inputs and outputs the volumetric leakage rate at each leakage location. Figure 12 shows a screenshot of the HTML CFM calculator, with inputs for pressure drop and flow coefficients on the right and outputs shown in the bar chart and on the bottom left.

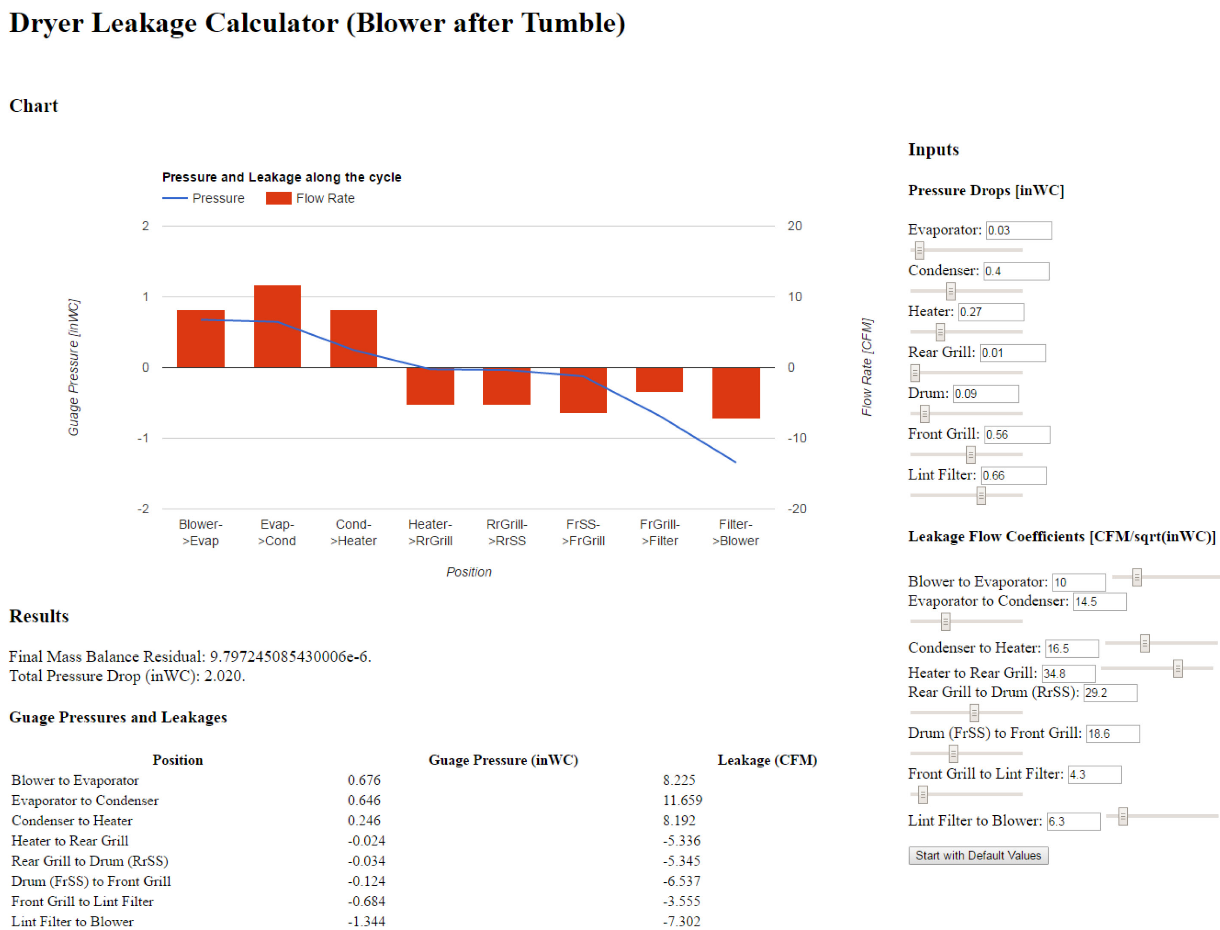

Figure 12. Example screenshot of HTML leakage calculator.

The methodology used in this HTML simultaneous equation solver is explained as follows. We begin with a thought experiment (which will evolve into a realistic dryer leakage model).

First, consider a circular duct with a fan and negligible pressure drop in the duct, as illustrated in Figure 13. Based on the fan curve and system curve, we can know the total flow rate (200 cfm) and pressure drop (0.01 in_{WC}) across the fan. However, we are not able to accurately predict the gauge pressure profile in the duct relative to ambient (note that the pressure plot has no fixed y-axis).

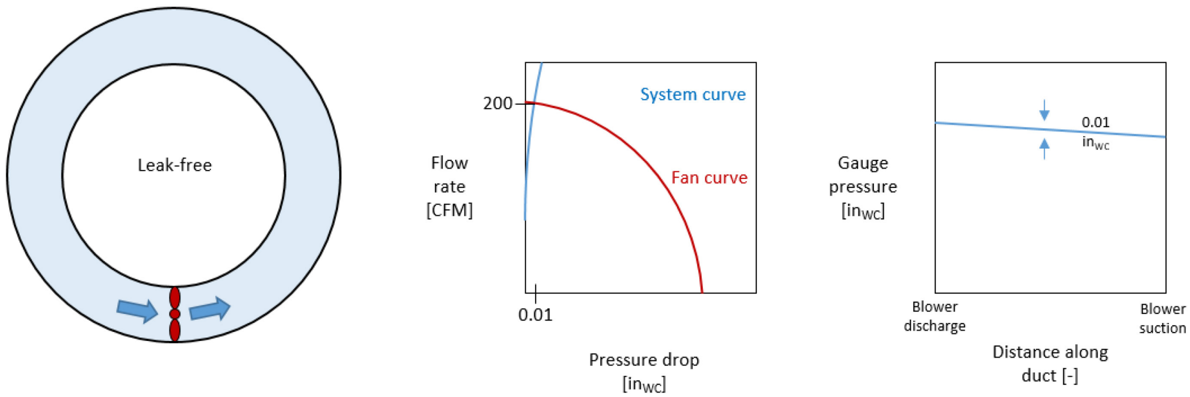

Figure 13. Leak-free circular duct with fan and negligible pressure drop.

Next, imagine that a series of discrete flow resistances (R1, R2…) with known pressure drops introduced, as illustrated in Figure 14. Knowing each resistance, we can continue to characterize the system curve and solve for the new flow rate (180 CFM) and blower pressure rise (2 in_{WC}). Now the shape of the pressure profile can be plotted against the discrete duct locations; however, we are still unable to accurately predict the gauge pressure profile in the duct relative to ambient (note that the pressure plot still has no fixed y-axis).

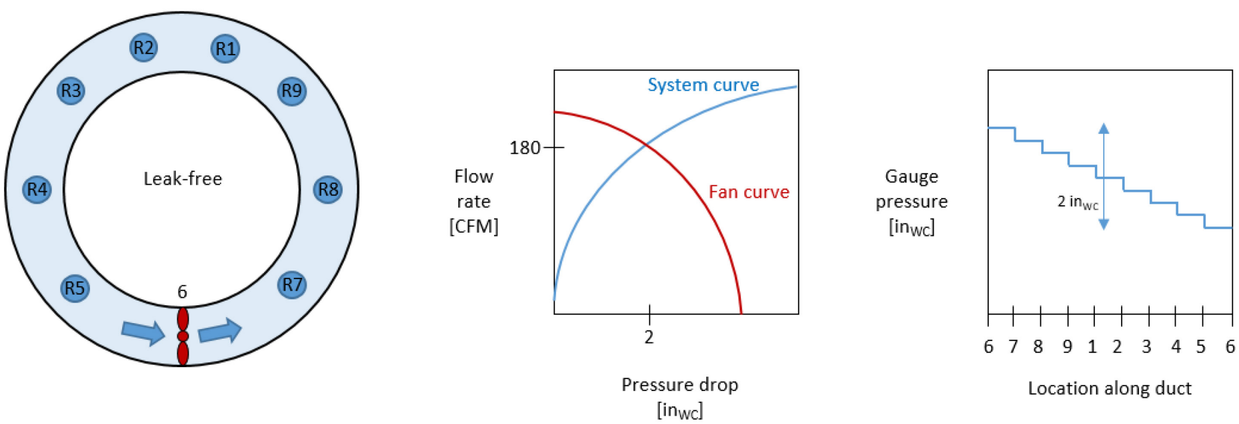

Figure 14. Leak-free circular duct with fan and a series of discrete non-negligible pressure drops.

Now we introduce one small leakage point ("small" is defined as "not large enough to substantially change the overall volume flow rate in the main duct flow"), as illustrated in Figure 15. Because the leak is small, the system curve and fan curve are not affected and are dropped from this and subsequent figures. The fundamental difference from the previous figure is that, in steady state, we are now able to locate the pressure relative to ambient. According to a mass balance, in steady state the flow through L6 must be zero. Since the C_v is non-zero, the pressure in this segment must be equal to the surroundings. Of course, to reach this steady state condition, the system will undergo a brief transient period in which the pressure everywhere rises or falls to its steady state value. However, the transient behavior is not of interest here, and we focus only on the steady state solution.

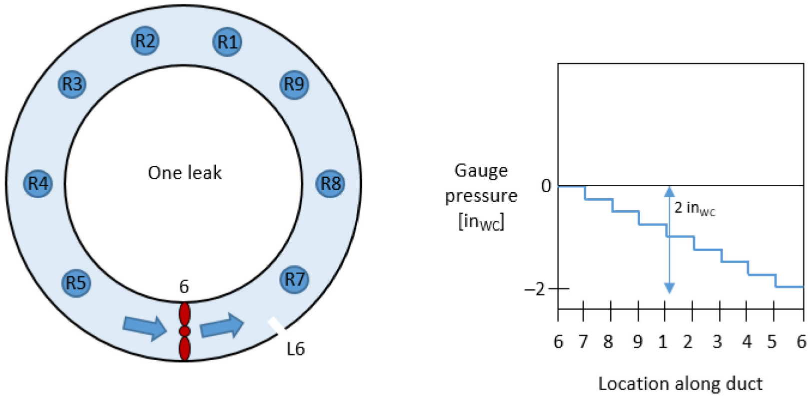

Figure 15. Circular duct with fan, a series of discrete pressure drops, and one small leak.

Next we add a second small leak, as illustrated in Figure 16. In the previous one-leak example, the pressure profile solution was trivial – we did not need to know the size of the single leak to solve for the pressure everywhere. However, the solution to the two-leak problem is no longer trivial – we need to know the size of each leak. By mass balance, we know the two flow rates must be equal and opposite. In case the leaks are of equal size (as drawn in Figure 16), we know that they must have equal and opposite gauge pressures, and we can solve the pressure profile without computation. However, if they are of unequal size (or if we want to know the leakage flow rate), we need to quantify their size and apply equations to solve for the pressure profile. These equations are written for the two-leak case below. The leakage "size" is quantified as a flow coefficient, or C_v value. The CFM of leakage flow will be proportional to the C_v value times the square root of pressure difference with ambient (ΔP), measured in inches water column. The unknown variables and the system of equations to solve for them are as follows:

29 variables for 9 segments:

- 9 gauge pressures (P_i for i=1 to 9)
- 2 leakage flow rates (V_6 and V_3)
- 8 ΔPs (component pressure drops, DP_i for i=1 to 8)
- 8 ΔP_{rel}'s (defined as the pressure difference between segment *i* and segment 1)
- 2 C_vs (C_{v6} and C_{v3})

11 known measured values:

- 8 ΔPs
- 2 C_vs

19 equations in a simultaneous system

- 3 governing equations:
  - 2 equations for volume flow: $V_i = \text{sign}(P_i)*Cv_i*\text{sqrt}(\text{abs}(P_{gage,i}))$ (for i=3, 6)
  - 1 equation for mass balance (constant density): $V_6 + V_3 = 0$ (free variable is $P_{gage,1}$)
- 16 conversion equations
  - 8 equations for i=1,8: $P_{gage,i+1} = P_{gage,1} + DP_{rel,i+1}$
  - 8 equations to define $DP_{rel,i+1} = DP_{rel,i} - DP_i$ (for i = 1 to 8)

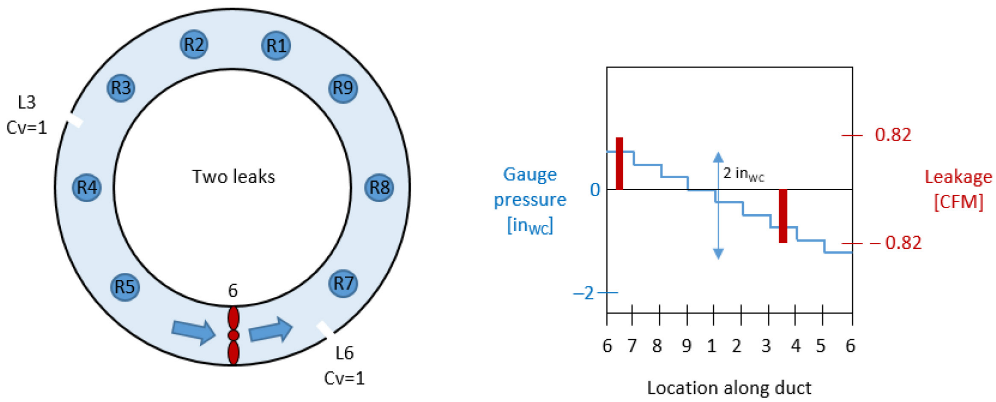

Figure 16. Circular duct with fan, a series of discrete pressure drops, and two small leaks.

Finally, we can open leakages at every segment as illustrated in Figure 17. The solution method can be genericized as outlined in the problem formulation below. This problem formulation will hold for an arbitrary number of segments, with arbitrary pressure drops and leakage sizes for each segment.

5N - 2 Variables for N segments:

- N gauge pressures (P_i for i = 1 to N)
- N leakage flow rates (V_i for i = 1 to N)
- N-1 ΔPs (component pressure drops, ΔP_i for i=1 to N-1)
- N-1 ΔP_{rel}'s (defined as the pressure difference between segment *i* and segment 1)
- N Cvs (Cv_i for i = 1 to N)

2N - 1 Known measured values:

- N-1 ΔPs
- N C_vs

3N - 1 Equations in a simultaneous system

- N + 1 Governing equations:
  - 1 equation for mass balance (constant density): $\sum V_i = 0$ (free variable is $P_{gage,1}$)
  - N equations for leakage flows: $V_i = \text{sign}(P_{gage,i}) * Cv_i * \text{sqrt}(\text{abs}(P_{gage,i}))$ (for i = 1 to N)
- 2N - 2 conversion equations
  - N-1 equations to find remaining P_{gage}'s: $P_{gage,i+1} = P_{gage,1} + \Delta P_{rel,i+1}$ (for i=1 to N-1)
  - N-1 equations to define $\Delta P_{rel,i+1} = \Delta P_{rel,i} - \Delta P_i$ (for i = 1 to N-1)

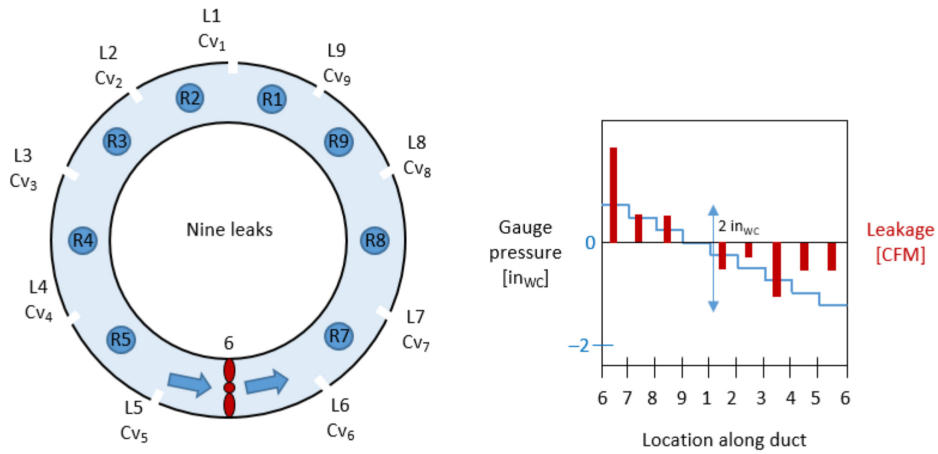

Figure 17. Circular duct with fan, a series of discrete flow resistances (component pressure drops), and an equal number of leakage locations of varying size.

With a C_v included between each component of flow resistance, we have now reached the level of leakage complexity of a clothes dryer (excepting the psychrometric heat and moisture transfers), and we can replace the "circular duct" with a HPCD diagram, as shown in Figure 18. Note that the C_v of the drum itself was taken as zero and left out, leaving an offset in the numbering nomenclature between C_v2-C_v8 and components numbered 3–9.

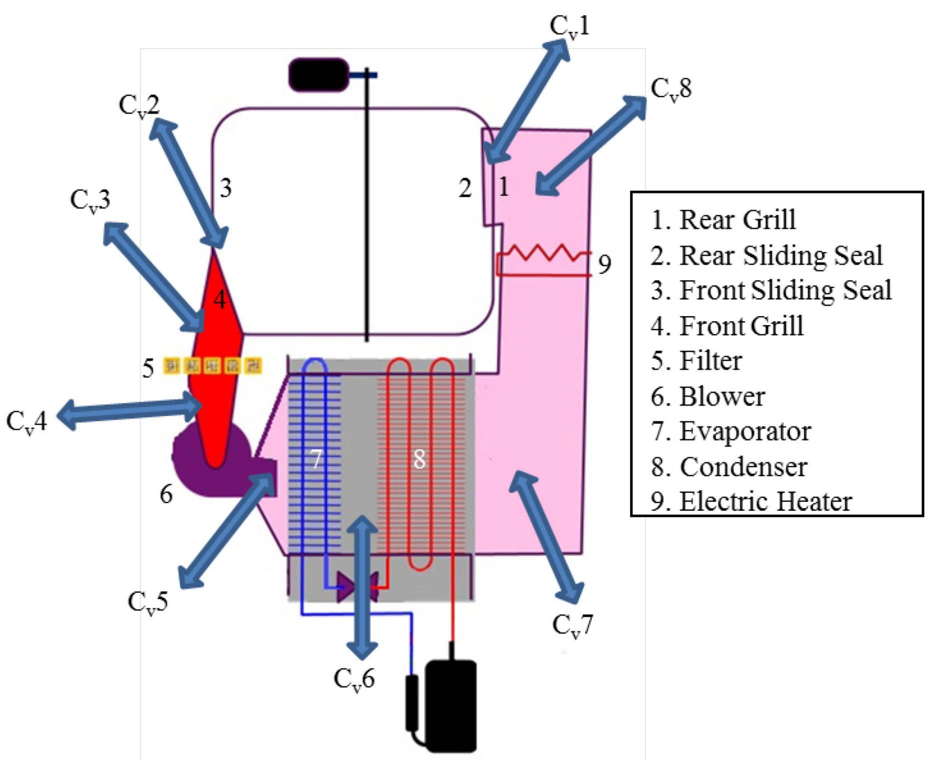

Figure 18. Flow-restriction components and leakage segments of the second generation prototype dryer.

In this project, the system of leakage equations was solved in an Engineering Equation Solver (EES)–based calculator. This EES version was also coupled to the thermodynamic and psychrometric cycle. In addition, a lightweight HTML-based calculator was developed for convenience during the project. Both these solvers can solve for the pressure profile and leakage rates for a measured set of C_vs and ΔPs. An example of the HTML calculator output is shown in Figure 19.

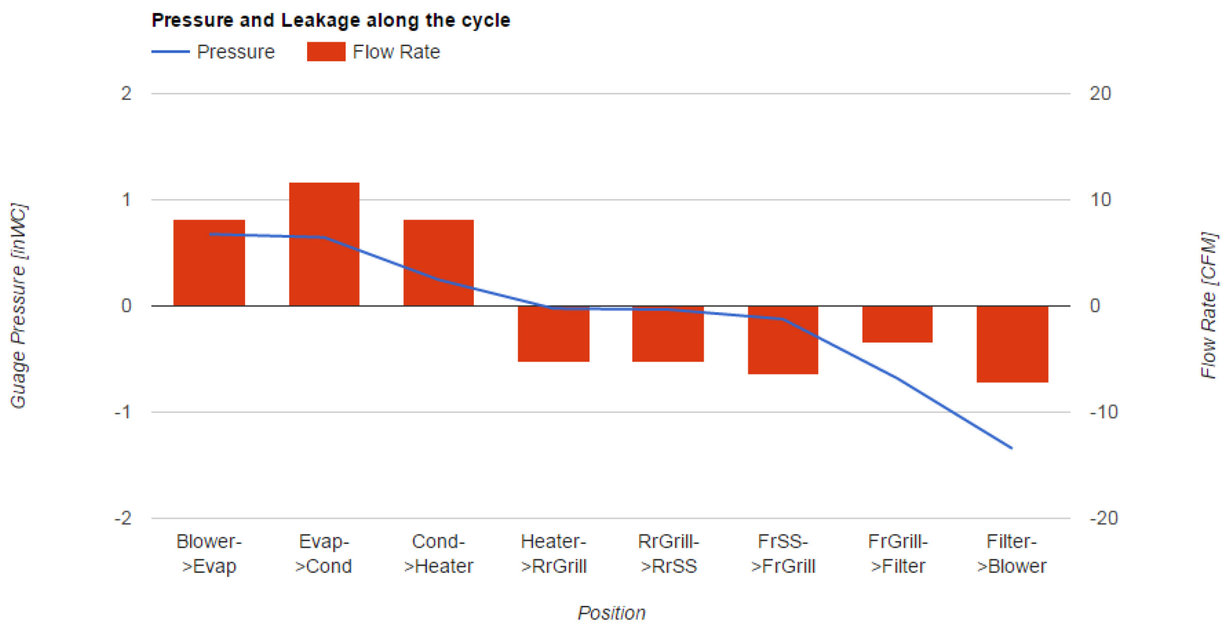

Figure 19. Example output of the HTML-based leakage calculator, showing pressure profile and leakage rates for a given set of measured C_vs and ΔPs relevant to the second generation HPCD prototype.

3.4.2 Results

Table 11 shows the total leakage of the HPCD for the first and second generations. The "total leakage" is a single measurement of whole-dryer leakage with blower and drum turned off. In other words, the entire dryer air system is pressurized (with no supplemental sealing) to gauge the "overall" leakiness of the dryer.

Table 11. Total leakage for the each prototype generation with static drum

Prototype Generation	Total C_v
Gen 1	140
Gen 2 (As-received)	143
Gen 2 (Sealed)	97
Gen 2 (Outdoor blower – Sealed)	108

Figure 20 shows the change in C_v for each leakage location (see Table 7 for key of C_v locations) in the second generation prototype as it was sealed and modified with an outdoor blower. The "as-received" and "sealed" measurements were taken before test number 1. The "outboard blower sealed" measurements were taken between test numbers 25 and 26 (between Test matrix 2 and 3). In going from the as-received unit to post-sealed (this included taping seams and transitions that could leak), all C_vs decreased or stayed the same. Major areas where leakage was improved were between the condenser and rear duct which housed the resistance element for supplemental heating and the duct between the blower and the evaporator. For the post-sealed unit, the factory blower was used.

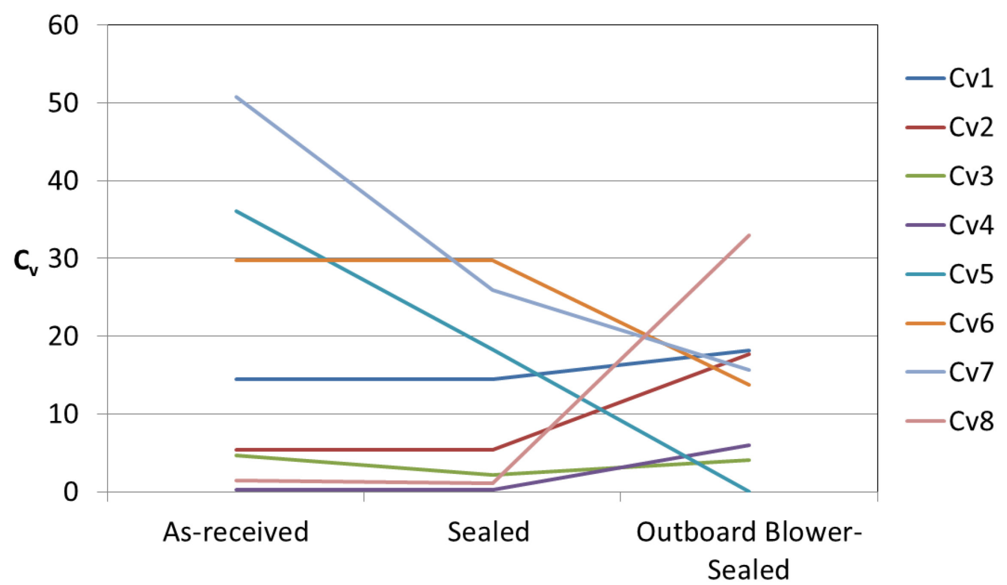

Figure 20. Change in C_v at all leakage locations in airflow path due to sealing activities.

The next iteration of the second generation unit included an outboard blower to provide more airflow. To accomplish this, a dryer door was fabricated with the bottom half cut out to allow flexible duct to run to and from the outboard blower. Figure 21 shows this prototype. In comparing the inboard blower sealed C_v results to the outboard blower results, notice that some C_vs increase and some decrease. The sliding seal C_vs (1 and 2) both increase; this is due to the modified front panel of the dryer to accommodate the ducting for the outboard blower. The modified door does not provide as much rigidity to the sliding seals as the complete original door, increasing their leakage.

Comments on the changes from "sealed" to "outboard blower sealed":

C_v1,2: sliding seals need to be measured dynamically (with rotation) and static measurements are notoriously variable

C_v3: (no issue)

C_v4,5: hardware changes were made, and the changes in C_v were expected

C_v6: better sealing was applied

C_v7: an improved gasket material was used

C_v8: compared to "sealed" measurement, "outboard blower sealed" measurement includes half of miscellaneous leakage from rear duct. C_v could also include front door seal leakage (different measurement procedure could have introduced this additional leakage).

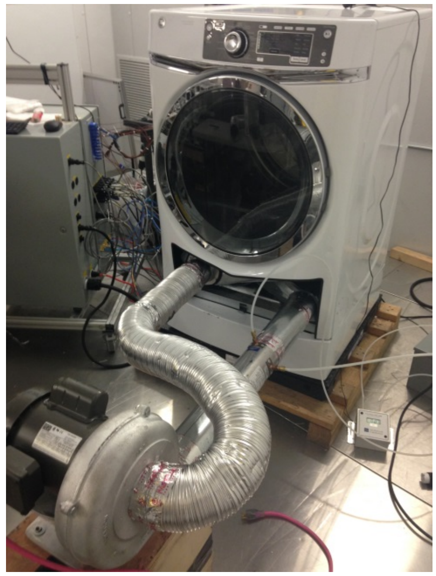

Figure 21. Outboard blower setup required the bottom of the front panel of the HPCD to be cut out.

Having the ducts to the outboard blower easily accessible to seal meant that the blower to evaporator (C_v5) was essentially brought to zero. New gaskets between the condenser and the rear duct with the heater decreased C_v7. Changing one C_v, increasing or decreasing the leakage area of one component, can change the leakage characteristics of the whole system.

Table 12 shows the C_vs between all state points for the baseline case (considered as "outboard blower-sealed" in Figure 20) as well as for a matrix of test with leakage points C_v1 and C_v5 increased). The baseline case had a total C_v of 114 with a total average CFM after the blower of 179 CFM at ~ 2.2 in. W.C. static pressure.

Table 12. Measured C_v for leakage points in HPCD air loop

C_v [CFM/√in WC]						
	Baseline	**Blower to Evap + 10**	**Blower to Evap + 20**	**Rear Grill +10**	**Rear Grill +20**	**Blower to Evap +10, Rear Grill +10 C_v**
Blower to Evap	0.0	10.0	20.0	0.0	0.0	10.0
Evap to Cond	14.5	14.5	14.5	14.5	14.5	14.5
Cond to Heater	16.5	16.5	16.5	16.5	16.5	16.5
Heater to Rear Grill	34.8	34.8	34.8	34.8	34.8	34.8
Rear Grill to Drum (RrSS)	19.2	19.2	19.2	29.2	39.2	29.2
Drum (FrSS) to Front Grill	18.6	18.6	18.6	18.6	18.6	18.6
Front Grill to Lint Filter	4.3	4.3	4.3	4.3	4.3	4.3
Lint Filter to Blower	6.3	6.3	6.3	6.3	6.3	6.3

The measured pressure drops from Table 10 with pressure drops measured during complete EF tests are combined in Table 13 for a complete picture of the characteristics of leakage and resistance to airflow in the air loop path.

Table 13. Measured pressure drops across resistive components

	Evaporator	Condenser	Heater	Rear Grill	Drum	Front Grill	Filter
Pressure drop [in WC]	0.033	0.369	0.274	0.012	0.093	0.562	0.658

The leakage and pressure drop information can be combined, and using the HTML CFM calculator, the volumetric flow rate at each leakage location can be computed. Table 14 shows these results.

Table 14. Predicted leakage from each leakage component

	Leakage [CFM] from HTML calculator					
	Baseline	**Blower to Evap + 10**	**Blower to Evap + 20**	**Rear Grill +10**	**Rear Grill +20**	**Blower to Evap +10, Rear Grill +10 C_v**
Blower to Evap	0	8.174	15.792	0	0	8.225
Evap to Cond	11.85	11.583	11.171	11.864	11.869	11.659
Cond to Heater	8.54	8.051	7.258	8.565	8.574	8.192
Heater to Rear Grill	-1.593	-6.218	-9.625	-0.801	0.089	-5.336
Rear Grill to Drum (RrSS)	-2.112	-3.931	-5.647	-2.996	-3.919	-5.345
Drum (FrSS) to Front Grill	-5.943	-6.756	-7.814	-5.897	-5.882	-6.537
Front Grill to Lint Filter	-3.499	-3.577	-3.69	-3.495	-3.493	-3.555
Lint Filter to Blower	-7.244	-7.325	-7.445	-7.24	-7.238	-7.302

Figure 22 shows visually the leakage for the baseline case.

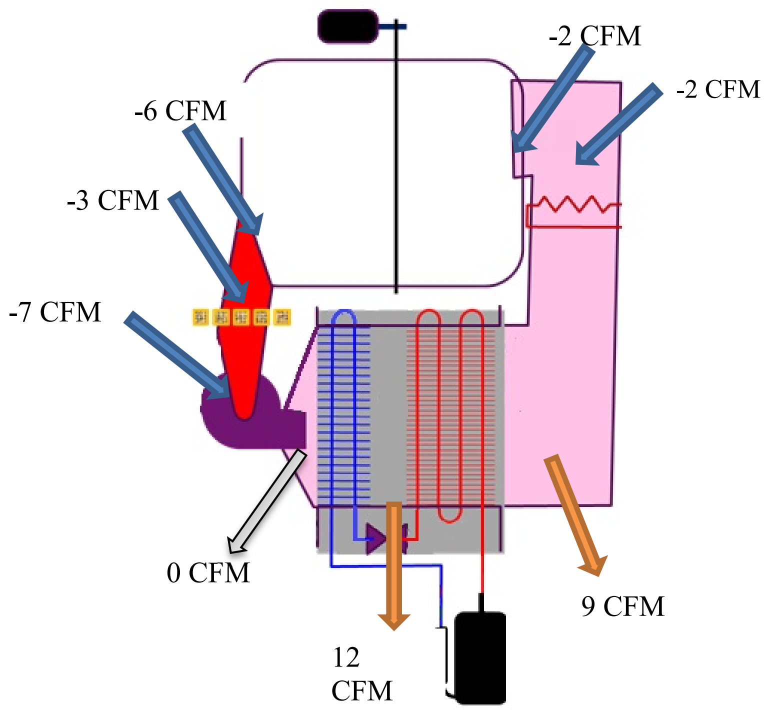

Figure 22. The baseline leakage of the outboard blower setup.

The HTML CFM calculator outputs the gauge pressure that can be compared to measurements for validation of the tool. Table 15 shows the output of the tool compared to measured values for the baseline case.

Table 15. Comparison of HTML CFM calculator predicted gauge pressure to measured pressure

	HTML CFM Calculator Gauge Pressure [inWC]	Measured Gauge Pressure [inWC]	Difference [inWC]	Difference as fraction of fan head [%]
Blower to Evap	0.698	0.641	+0.057	+2.8%
Evap to Cond	0.668	0.609	+0.059	+2.9%
Cond to Heater	0.268	0.238	+0.03	+1.5%
Heater to Rear Grill	-0.002	-0.034	+0.032	+1.6%
Rear Grill to Drum (RrSS)	-0.012	-0.033	+0.021	+1.0%
Drum (FrSS) to Front Grill	-0.102	-0.122	+0.02	+1.0%
Front Grill to Lint Filter	-0.662	-0.725	+0.063	+3.1%
Lint Filter to Blower	-1.322	-1.308	-0.014	-0.7%

Using the measured DPs and C_vs, the gauge pressure profile of the system was predicted within 0.06 in. WC for all state points. This represents about 3% of the fan head (2 in. WC).

3.5 MODEL DEVELOPMENT – GENERAL

Three models of the HPCD were developed in this project, as detailed in Table 16. Each has its own section in this report. First, this section covers general elements of the modeling that impacted all of the models (and are applicable no matter the dryer modeling platform chosen). Section 3.6 deals with the HPDM-based HPCD model, Section 3.7 covers the EES-based HPCD model, and Section 3.8 covers the HTML-based leakage model.

Note that the EES model was completely stand-alone. The HPDM model was more sophisticated with respect to the vapor compression components, and requires leakage inputs from the HTML or EES-based model.

Table 16. Models developed in this project

Modeling platform and description	Coupled systems	Key model outputs	Vapor compression cycle model	Leakage model	Drum model
HPDM	Psychro Thermo	CEF, dry time, compressor discharge temperature	Equipment-based, detailed compressor map, segmented heat exchangers	Leakage CFMs input for each case from HTML calculator	Effectiveness based
EES	Psychro Thermo Leakage	CEF, dry time, leakage profile	Approach temperature-based. COP as a fraction of Carnot limit; capacity proportional to suction density	Simultaneous equation solution based on measured C_vs and DPs	Fixed drum outlet RH
HTML	Leakage	Leakage profile	N/A	Simultaneous equation solution based on measured C_vs and DPs	N/A

3.6 HPDM MODEL DEVELOPMENT

3.6.1 General Introduction of ORNL Heat Pump Design Model

ORNL Heat Pump Design Model (HPDM, Rice 1997 and Shen and Rice 2014) is a well-recognized, public-domain HVAC equipment modelling and design tool. It has a free web interface to support public use, which has been accessed over 300,000 times by US and worldwide engineers. HPDM is used as the major base of our design work, to compare system configurations, select components, and size heat exchangers.

The ORNL Building Equipment Research team has over 30 years of experience in thermal system and component modeling. We have developed in-house steady-state simulation models covering most categories of residential and light commercial space cooling, space heating, and water heating components, like compressors, heat exchangers, pumps, fans, etc. These models have been extensively used and validated through our research projects. Being different from the performance curves used in EnergyPlus and other building energy simulation software, our models are fundamentally based, can simulate detailed heat exchanger geometry and circuitry, and accept real air side and refrigerant side boundary conditions. These models are actually equipment design tools, which can do performance prediction, component sizing, and system optimization at specified efficiency levels and cost.

Our in-house heat exchanger models have different complexity levels, falling under three categories, i.e., bulk models, phase-to-phase models, and discretized models. The bulk models are usually based on Effectiveness-NTU (number of transfer units) or UA-LMTD (overall heat transfer-log mean temperature difference) approach, to simulate the component as a whole. The phase-to-phase models separate the refrigerant side to vapor, two-phase, and liquid regions, and each region has individual air side and refrigerant side entering states. The discretized models use segment-to-segment modeling approach, which divide a heat exchanger into numerous mini-segments; each segment has individual refrigerant and air entering parameters and considers possible phase separation; the mini-segments are basic building blocks, which are used to build up heat exchangers having arbitrary circuitry, geometry, and represent any boundary conditions. All our phase-to-phase and segment-to-segment heat exchanger models are able to calculate refrigerant charge inventory. For the high-efficiency rooftop unit (RTU) development project, we particularly enhanced our segment-to-segment heat exchanger modeling capacity, so as to serve the needs for modeling large complicated heat exchangers like interlaced fin-tube coils and micro-channel heat exchangers. Some relevant component models and features in the HPDM library are introduced as below:

Compressors:

Single-speed compressor: We use AHRI 10-coefficient compressor maps (ANSI/AHRI 540-99, 2010) to calculate mass flow rate and power consumption and enable calculation of the refrigerant-side vs. air-side energy balance from inlet to outlet. We also consider the actual suction state to correct the map mass flow prediction using the method of Dabiri and Rice (1981) as given in Eq. 3.

Variable-speed compressor: The model accepts multiple sets of mass flow and power curves and does linear interpolation between speed levels.

$$\dot{m}_{ref,actual} = [1 + F_{mass}(\frac{v_{ARI-map}}{v_{act}} - 1)]\dot{m}_{ref,ARI-map} \quad , \qquad \text{Eq. 3}$$

where F_{mass} is an empirical correction factor assigned a value of 0.75, $\dot{m}_{ref,ARI-map}$ and $\dot{m}_{ref,actual}$ are the mass flow rates at the standard (compressor map) and actual suction superheat, and $v_{ARI-map}$ and v_{act} are the specific volumes at the standard and actual superheat.

In the case of the HPCD application, the very high evaporating temperature is beyond typical compressor map conditions. Thus no AHRI 10-coefficient compressor maps are directly available for compressors. To overcome this difficulty, we used basic efficiencies to model the compressor, i.e., volumetric efficiency, as shown in Eq. 4, and isentropic efficiency, as shown in Eq. 5.

$$m_r = Volume_{displacement} \times Speed_{rotation} \times Density_{suction} \times \eta_{vol} \, , \qquad \text{Eq. 4}$$

$$Power = m_r \times (H_{discharge,s} - H_{suction}) / \eta_{isentropic} \, , \qquad \text{Eq. 5}$$

Where m_r is compressor mass flow rate; $Power$ is compressor power; η_{vol} is compressor volumetric efficiency; $\eta_{isentropic}$ is compressor isentropic efficiency; $H_{suction}$ is compressor suction enthalpy; and $H_{discharge,s}$ is an enthalpy obtained at the compressor discharge pressure and suction entropy.

Heat Exchangers:

Segment-to-segment fin-and-tube condenser: A segment-to-segment modeling approach is used. Each tube segment has individual air side and refrigerant side entering states and considers possible phase transition. An ε-NTU approach is used for heat transfer calculations within each segment. The air-side fin is simplified as an equivalent annular fin. Both refrigerant and air-side heat transfer and pressure drop are considered; the coil model can simulate arbitrary tube and fin geometries and circuitries and any refrigerant-side entering and exit states, misdistribution and accept two-dimensional air-side temperature, humidity, and velocity local inputs. The tube circuitry and 2-D boundary conditions are provided by an input file.

Segment-to-segment fin-and-tube evaporator: In addition to the functionalities of the segment-to-segment fin-tube condenser, the evaporator model is capable of simulating dehumidification process. The method of Braun et al. (1989) is used to simulate cases of water condensing on an evaporating coil, where the driving potential for heat and mass transfer is the difference between enthalpies of the inlet air and saturated air at the refrigerant temperature.

Expansion Devices:

Idealized TXV: The compressor suction superheat degree is explicitly specified.

Fans and Blowers:

Single-speed fan: Given the airflow rate, the model uses a fan curve to simulate static head, power consumption, and calculate air-side temperature increment from inlet to outlet.

Refrigerant Properties:

Interface to Refprop 9.0: We programmed interface functions to call Refprop 9.0 directly. Our models accept all the refrigerant types in the Refprop 9.0 database, and we can also simulate new refrigerants by making the refrigerant definition file according to the Refprop 9.0 format.

Refprop 9.0 can be fairly slow. To speed up the calculation, we have an option to generate hybrid property look-up tables, based on Refprop 9.0. Our program uses 1-D and 2-D cubic spline algorithms to calculate refrigerant properties via reading the look-up tables. This would greatly boost the calculation speed, given the same accuracy; however, the cubic spline algorithms are less accurate when approaching to the critical region, in which case we switch back to the Refprop 9.0 functions.

Optimization:

HPDM has embedded optimization capability, which uses GenOpt, an open source optimization program published by Wetter (2009). A wrapper program was developed to communicate between GenOpt and HPDM by exchanging text input and output files. The GenOpt optimization wrapper is shown in Figure 23. GenOpt automatically generates input files for the simulation program based on predefined templates that include keywords describing the problem variables.

As shown in Figure 23, the problem domain is defined in two parts. One part defines required inputs for the GenOpt program (in the GenOpt command file), which selects the optimization algorithm and regulates design spaces for the iterative variables; the other part (in the wrapper template file) defines attributes and design spaces for the selected objectives. The wrapper program accepts three kinds (attributes) of objectives: optimization objectives, target objectives (equality constraints), and bound objectives (inequality constraints). An optimization objective is to maximize or minimize an output variable, a target objective intends to match the output variable to a given value, and a bound objective is to define upper and lower bounds for an output variable.

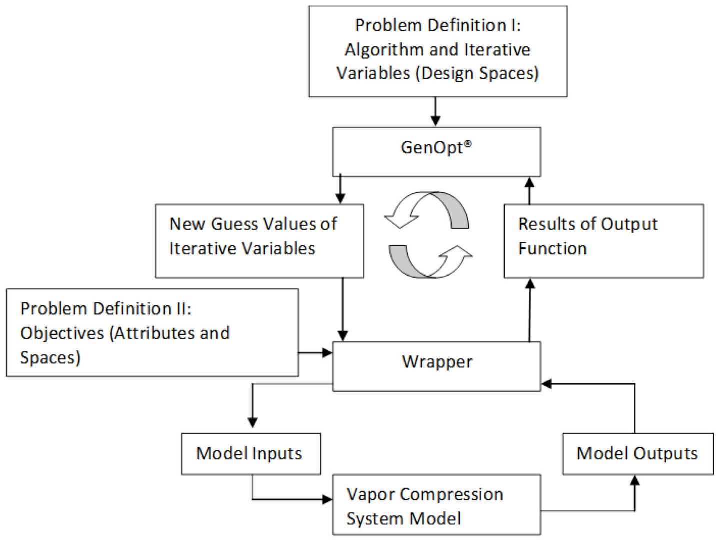

Figure 23. GenOpt Optimization Wrapper to a Vapor Compression System Model.

GenOpt produces guess values for the iterative variables through a text file to the wrapper program. The wrapper program interprets the input file to provide the required inputs for the vapor compression system model and then executes the model to get performance outputs. Then, the wrapper program provides the outputs in the form shown in Eq. 6.

$$f(x) = \sum(W_i * OptObj_i) + \sum[T_j * (TgtObj_j - Goal_j)]^2 + \sum[P_k * (BndObj_k - Bound_k)]^2 \quad \text{Eq. 6}$$

where $f(x)$ is the integrated function to be minimized by the GenOpt algorithm, x is a vector of the model variables to be iterated, and W_i is the weighting factor for an optimization objective. $OptObj_i$ is a variable for optimization. It will be maximized by giving a negative weighting factor and minimized by giving a positive weighting factor. $TgtObj_j$ is a variable intended to match a given target value, and T_j is a weighting factor to be multiplied with the residual. $Goal_j$ is a given target value. $BndObj_k$ is an output variable having either upper or lower bound. $Bound_k$ is a given boundary value. P_k is a penalty factor, which is zero when the output variable is within the given bounds; on the other hand, it becomes a quite large multiplier when the output variable goes beyond the bounds.

Next, GenOpt evaluates the result of the output function and updates the guesses for the iterative variables. The interaction process between GenOpt and the wrapper program is repeated until the minimum of the output function is found. For the analyses below, the optimization algorithm applied was Generalized Pattern Search algorithm (Hooke-Jeeves and Coordinate Search algorithm).

3.6.2 **Dryer Drum Model**

A new approach was taken to model the drum in which the heat and mass transfer effectiveness model for wet cooling towers was adapted to the case of the clothes tumbler drum. Such an approach had also proved capable of modelling another adiabatic evaporative air cooling process through wetted porous media: in the study by Ally and Shen (2010), an evaporative precooling pad for condenser evaporative precooling was analyzed. The clothes load is to similar to the precooling pad, thus, the modelling approach is adopted here.

In this flexible effectiveness modeling framework, the drum is characterized by an "effectiveness," rather than having to assume a particular leaving humidity. This model framework allowed empirical evaluation of the drum effectiveness to improve the extrapolative accuracy of the full system HPDM model.

Heat and mass transfer in the drum is the major transient process that has been modeled. The heat and mass transfer process is described below.

$$\omega_{out,i} = \omega_{surf,i} - (\omega_{surf,i} - \omega_{in,i}) \times (1.0 - E_M), \qquad \text{Eq. 7}$$

$$T_{out,i} = T_{surf,i} - (T_{surf,i} - T_{in,i}) \times (1.0 - E_H), \qquad \text{Eq. 8}$$

$$Q_i = m_{air,circ} \times \left(H_{out,i} - H_{in,i}\right), \text{ and} \qquad \text{Eq. 9}$$

$$WaterFlow_i = m_{air,circ} \times \left(\omega_{out,i} - \omega_{in,i}\right), \qquad \text{Eq. 10}$$

where

$\omega_{in,i}$ and $\omega_{out,i}$ are the air specific humidity entering and leaving the drum at moment *i* [lbm H_2O/lbm dry air],

$T_{in,i}$ and $T_{out,i}$ are the air temperatures entering and leaving the drum at moment *i* [°F],

$T_{surf,i}$ is the surface temperature of the clothes load in the drum at moment *i* [°F], and the clothes load is assumed to have a uniform temperature at each moment,

$\omega_{surf,i}$ is the specific humidity of the saturated air at the surface temperature of $T_{surf,i}$ [lbm H_2O/lbm dry air],

Q_i is the total heat and mass transfer rate at moment *i* [Btu/hr], and

$WaterFlow_i$ is the water rate pick up by the air stream at moment *i*.

E_M and E_H are the mass and heat transfer effectiveness, respectively. By rearranging Equations 7 and 8, they can be defined as

$$E_M = 1 - \frac{\omega_{surf,i} - \omega_{out,i}}{\omega_{surf,i} - \omega_{in,i}} \text{ and} \qquad \text{Eq. 11}$$

$$E_H = 1 - \frac{T_{surf,i} - T_{out,i}}{T_{surf,i} - T_{in,i}}. \qquad \text{Eq. 12}$$

The above equation set is incomplete: one more measurement or equation is required. As a simplification, it is assumed that E_M is equal to E_H which allows the equation set to be solved. This assumption is analogous to assuming a Lewis number (dimensionless ratio of thermal to mass diffusivity) of unity. The assumption deserves a more detailed and fundamental study in the future.

Using the assumption of equal heat and mass transfer effectiveness, effectiveness was obtained from laboratory measured data, specific to a particular drum, circulation airflow rate, and the standard clothes load. The figure below shows the heat and mass transfer effectiveness as a function of RMC, defined as remaining water weight per unit dry cloth weight. The RMC was known based on measurements of a high-precision whole-dryer scale, and effectiveness was calculated based on measurements of drum inlet and outlet temperatures, with the assumption that $E_M = E_H$. It can be seen in Figure 24 that the effectiveness increases almost linearly with the RMC. The strong dependence of the effectiveness on the RMC indicates that the equations 4 to 7 capture the major physics.

The empirically measured effectiveness of the drum for one run of the first generation dryer is shown in Figure 24.

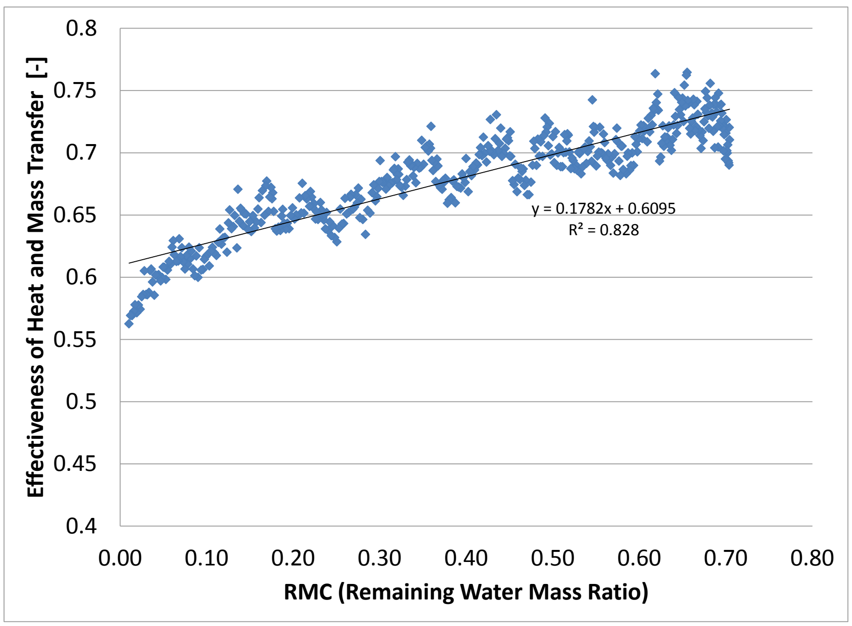

Figure 24. Drum heat and mass transfer effectiveness as a function of RMC for one run of the first generation HPCD prototype.

3.6.3 HPDM Quasi-Steady-State Heat Pump Clothes Dryer System Model

Heat pump clothes dryers apply vapor compression systems in the clothes drying application. A HPCD uses the evaporator to condense water and recovers condenser energy to heat clothes load. It does not require a venting duct through a building wall.

A schematic of a HPCD is shown in Figure 25, while detailed schematics and the operation principle are illustrated in Figure 26. A heat pump is a mechanical vapor compression refrigeration system consisting of primarily four main components, namely, an evaporator (7), a compressor (4), a condenser (5), and an expansion valve (9). The processed air is recirculated in the cycle continuously until drying is complete. Following Figure 26, the heated and dried air enters the clothes drum at state 1. It extracts the moisture from the wet clothes in the drum at state 2, where its temperature decreases and its relative humidity increases. At the drum exit at state 3, the air is almost saturated, at least in the initial stages of drying. The warm (i.e., relatively cooler) and moist air proceeds through the lint screen and flows over the evaporator of the vapor compression refrigeration system at state 7. Due to the low-temperature refrigerant flowing inside the evaporator coil, a significant amount of moisture from the air is condensed out at state 8 and is collected in a tray, while the drier and cooler air is blown by the fan at state 6 over the condenser of the vapor compression system. The drier air gets heated due to the hot refrigerant flowing inside the condenser and is fed back to the drum at state 1. Thus the net effect is that moisture evaporated from the wet clothes is condensed at the evaporator. This cycle continues until full drying is accomplished.

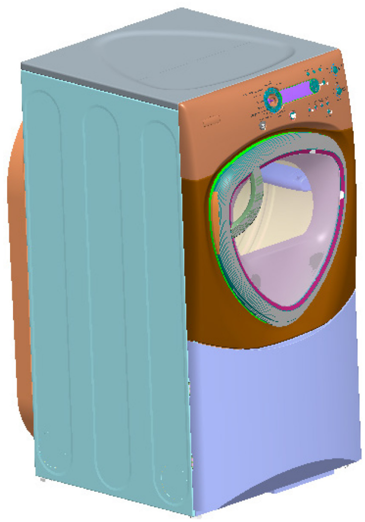

Figure 25. View of a heat pump dryer.

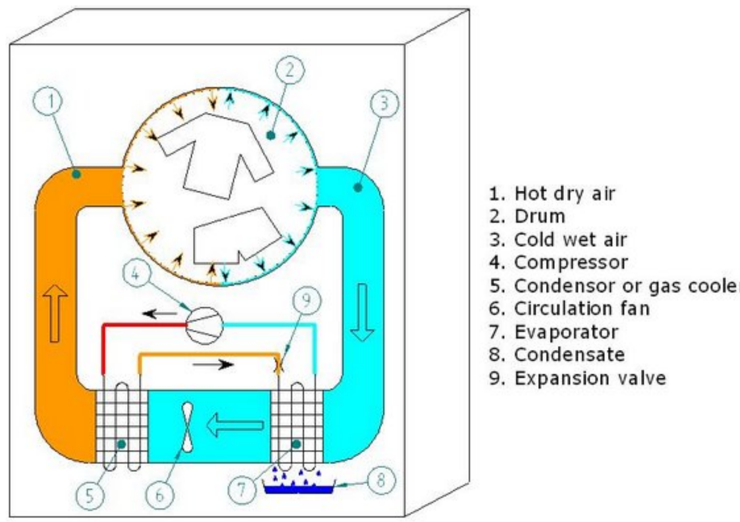

Figure 26. Schematics of a heat pump clothes dryer.

Clothes drying in a HPCD is a transient process. In one complete airflow path, the air stream circulates through the evaporator, condenser, circulation fan, drum, and ducts. In the condenser, the air temperature is increased and the specific humidity is unchanged; after that the air passes the drum to pick up moisture. Due to the evaporative cooling effect, the air temperature decreases through the drum. The HPCD is a closed system. Energy is added to the control volume as electric power to the compressor, circulation fan, and the drum rotator, and energy leaves the control volume by the condensate water, heat loss to the surrounding air, and air leakages in and out of the flow path. In the beginning of a drying process, the energy leaving the system is lower than the energy added. As a result, the internal air heats up, and the compressor suction and discharge pressures increase. Later in the drying process, as the drier clothes provide less of an evaporative cooling load in the drum, compressor suction and discharge pressures increase further. As shown in Figure 27, air circulation starts at a low temperature and humidity and ends at a high temperature and humidity. It is a critical design consideration to prevent overheating the compressor, i.e., limiting the compressor discharge temperature before the clothes are fully dry.

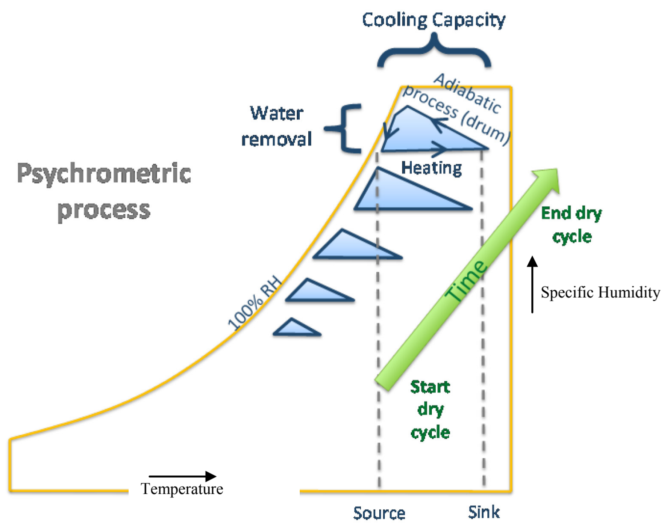

Figure 27. Transient clothes drying process in a psychrometric chart.

The standard metric for dryer performance in the United States is the energy factor, as defined in Eq. 13.

$$\textit{Energy Factor} = \frac{\textit{Weight of dry clothes}}{\textit{Energy consumed to dry them}} \qquad \text{Eq. 13}$$

The minimum CEF of an electric dryer required by the 2015 DOE minimum efficiency standard is 3.73 lb/kWh. DOE’s MYPP goal is to be higher than 6.0. During a standard CEF test, the initial moisture content (MC), defined as the ratio of water weight divided by dry clothes weight, is 57.5%, and the final MC is 4%. The total dry timing is also an important design target.

It can be seen from above, that designing a HPCD involves complicated physics, i.e., sizing heat exchangers, airflow rate, and compressor for better efficiency and lower cost, predicting EF and total drying time and estimating the maximum compressor discharge temperature in the transient drying process. Ling (2013) used CoilDesigner to design heat exchangers for a two-stage HPCD, which is a good example for modeling the HPCD at the component level. However, a complete HPCD system model, able to integrate all the components and simulate the transient process, is still absent. The paper (Ling 2013) introduces the development of a first-of-its-kind, quasi-steady-state HPCD system model based on detailed hardware-based component information and first principle.

Development of the HPCD system model was implemented in an existing, steady-state vapor compression system model, i.e., the ORNL Heat Pump Design Model (HPDM), with the addition of new HPCD features and components of drum, duct heat loss. HPDM was improved to simulate the quasi-steady-state process by assuming the vapor compression system reaches steady state at each individual time step. A time step is determined to reach a temperature increment in the clothes load (e.g., 0.1 K). The transient element (the drum model) updates the boundary condition to the steady-state heat pump system, and drives a new system balance state at each time step. Thus the vapor compression model was steady state, and the drum model was transient. The drum and clothes load are modeled with thermal masses, and the drum effectiveness was also a function of RMC.

The RMC and clothes load surface temperature change for each time step, and result in changing air temperature and humidity to the vapor compression system. Quasi-steady state simulations mean that we calculate steady-state vapor compression system balance points within each time step, and the transient drum model drives the time-dependent boundary conditions.

Transient Heat and Mass Transfer Process in the Drum:

Heat and mass transfer in the drum is the major transient process that has been modeled. The heat and mass transfer process is described below [Braun et al. (1989)].

$$\omega_{out,i} = \omega_{s,i} - (\omega_{s,i} - \omega_{in,i}) \times (1.0 - E_M), \quad \text{Eq. 14}$$

$$T_{out,i} = T_{s,i} - (T_{s,i} - T_{in,i}) \times (1.0 - E_H), \quad \text{Eq. 15}$$

$$Q_i = m_{air,circ} \times (H_{out,i} - H_{in,i}), \text{ and} \quad \text{Eq. 16}$$

$$WaterFlow_i = m_{air,circ} \times (\omega_{out,i} - \omega_{in,i}), \quad \text{Eq. 17}$$

where

$\omega_{in,i}$ and $\omega_{out,i}$ are the air specific humidity entering and leaving the drum at moment *i* [lbm H_2O/lbm dry air].

$T_{in,i}$ and $T_{out,i}$ are the air temperatures entering and leaving the drum at moment *i* [°F],

$T_{s,i}$ is the surface temperature of the clothes load in the drum at moment *i* [°F], and the clothes load is assumed to have a uniform temperature at each moment.

$\omega_{s,i}$ is the specific humidity of the saturated air at the surface temperature of $T_{s,i}$ [lbm H_2O/lbm dry air],

Q_i is the total heat and mass transfer rate at moment *i* [Btu/hr], and

$WaterFlow_i$ is the water rate pick up by the air stream at moment *i*.

E_M and E_H are the mass and heat transfer effectiveness, respectively. As a simplification, it is assumed that E_M is approximately equal to E_H. Using this assumption, effectiveness was obtained from laboratory measured data, specific to a particular drum, circulation airflow rate, and the standard clothes load. The figure below shows the heat and mass transfer effectiveness as a function of RMC, defined as the remaining water weight per unit dry cloth weight. The RMC was known based on measurements of a high-precision whole-dryer scale, and effectiveness was calculated based on measurements of drum inlet and outlet temperatures, with the assumption that $E_M = E_H$.

Energy Balance between the Clothes Load and Air Stream:

Q_i is the energy rate carried away by the air stream in each moment; therefore, the remaining internal energy in the load is

$$\begin{aligned} M_{clothes} \times U_{clothes,i} + M_{water,i} \times U_{water,i} \\ = M_{clothes} \times U_{clothes,i+1} + M_{drum} \times U_{drum} + M_{water,i+1} \times U_{water,i+1} \\ + Q_i \times \Delta Time \,, \end{aligned} \quad \text{Eq. 18}$$

where

$M_{clothes}$ is the thermal inertia mass [lbm] of the clothes (bone dry).

$M_{drum} \times U_{drum}$ is the enery change due to the thermal mass of the drum metal and other hardware.

$M_{water,i}$ and $M_{water,i+1}$ are the water weights in the load, at moment *i*, and the next moment of *i*+1 [lbm],

$\Delta Time$ is the time step between the moment *i* and *i*+1 [h],

$U_{clothes,i}$ = 0.32*$T_{s,i}$ is the internal energy of the clothes at moment i [Btu/lbm], and 0.32 [Btu/R/lbm] is the specific heat of the clothes load, i.e., assuming it is cotton.

$U_{water,i}$ is the water internal energy at moment i [Btu/lbm], which is a function of the load surface temperature $T_{s,i}$,

$M_{water,i}$ and $M_{water,i+1}$ are the water weight at moment *i* and moment *i*+1 [lbm], respectively. The relationship between them is given as

$$M_{water,i} = M_{water,i+1} + WaterFlow_i \times \Delta Time. \qquad \text{Eq. 19}$$

Heat Loss:

The heat losses upstream and downstream of the drum are modeled using simple effectiveness method, i.e.,

$$Heat\ Loss = E_{loss} \times m_{air,circ} \times Cp_{air} \times \left(T_{air,in,circ} - T_{air,enviro}\right), \qquad \text{Eq. 20}$$

where

$m_{air,circ}$ is the dry air circulation mass flow rate [lbm Dry Air/hr],

Cp_{air} is the air specific heat [Btu/°R/lbm Dry Air],

$T_{air,enviro}$ is the surrounding air temperature, which is assumed to be the same as the indoor temperature, i.e., 70°F,

$T_{air,in,circ}$ is the air temperature entering a heat loss section, i.e., upstream or downstream of the drum, and

E_{loss} is the heat transfer effectiveness. A UA value can be used as an alternative if it can be easily measured. We use the loss effectiveness here, because it is an easier value to guess.

Air-Side Leakages:

Air-side leakages are directly inputted as CFM to individual air-side points. For a point leaking out, the air stream subtracts the leaked flow rate and proceeds to the next state point with the reduced mass flow rate and temperature and humidity unchanged. For a point leaking in, the leaked surrounding air gets mixed with the moist air inside the system, the mixed air, with incremented flow rate, mixed temperature, and humidity flows to the next state point.

Quasi-Steady-State Simulation Steps:

For one time step, the quasi-steady-state simulation is conducted as follows and illustrated in Figure 28.

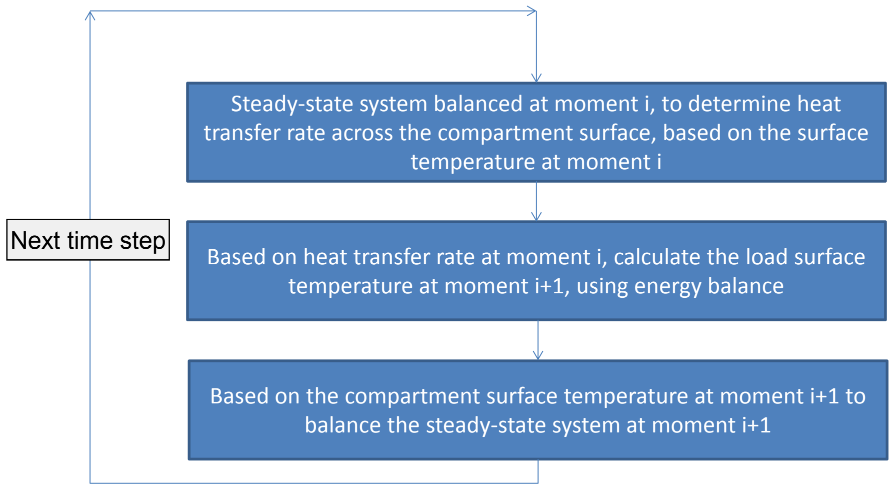

Figure 28. Quasi-steady-state time step.

Step 1 (top box in Figure 28): At the beginning of one time step, i.e., moment *i*, the vapor compression system model calculates the steady-state refrigerant-side state points based on the evaporator and condenser airflow rate and entering air temperatures and humidities. In addition, it calculates the water condensation rate and the air state exiting the condenser. Before entering the drum, the air stream picks up additional heat from the circulation fan and the drum rotator, while losing some heat to the environment. The energy transfers are treated as steady-state processes.

Step 2 (middle box in Figure 28): During the heat and mass transfer process in the drum, the warm air flows over the clothes load with the surface temperature at moment *i*. Using Eqs. 14 to 17, the heat transfer and water evaporation rates and the air outlet state are calculated. By multiplying the heat transfer rate and water evaporation rate by the time step duration, the moisture loss and internal energy change in the clothes load are determined. The internal energy and thermal mass changes lead to a new load surface temperature at moment *i*+1, as shown in the Eqs. 18 and 9.

Step 3 (bottom box in Figure 28): The air stream flows out of the drum, and the air temperature decreases due to the heat loss before entering the evaporator. The updated air temperature, humidity, and airflow rate entering the evaporator are the new air-side boundary conditions used for moment *i*+1, and the simulation goes back to step 1 with incrementing one moment.

3.6.4 Model Validation

Using the measured data from testing the latest version of GE HPCD, we reduced the component information. In comparison to the previous HPCD, the latest GE HPCD uses a smaller evaporator, condenser, and compressor. It changed the blower position from the drum entrance to the drum exit. Figure 29 depicts the system diagram (the arrows indicate potential air leakage points and directions).

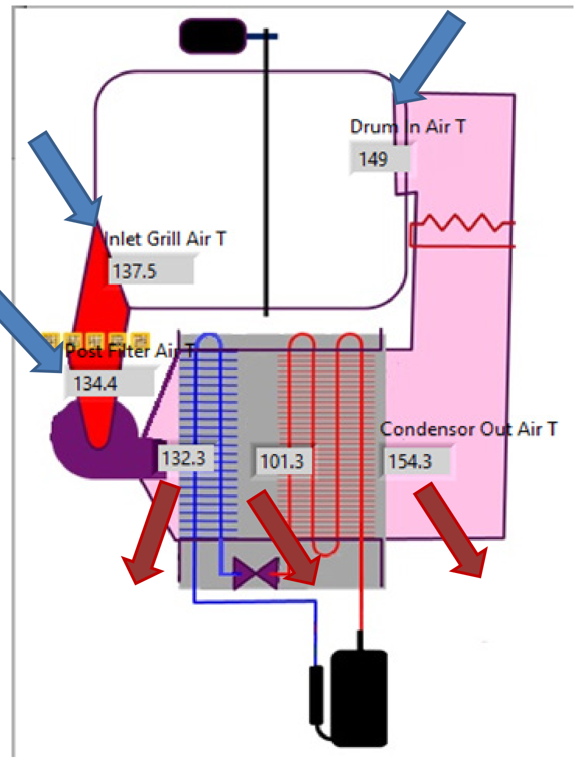

Figure 29. System diagram of GE heat pump clothes dryer.

We assume that heat transfer effectiveness is equal to mass transfer effectiveness. Using the experimental data, we first calculated the drum heat and mass transfer effectiveness as a function of the remaining moisture content (RMC) and compared it to the previous drum heat and mass effectiveness (Figure 30 and Figure 31). It can be seen that the new drum effectiveness is higher than the previous drum.

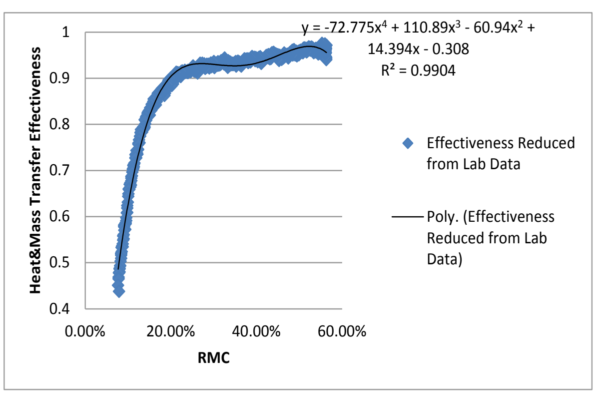

Figure 30. Heat and mass effectiveness of second generation drum.

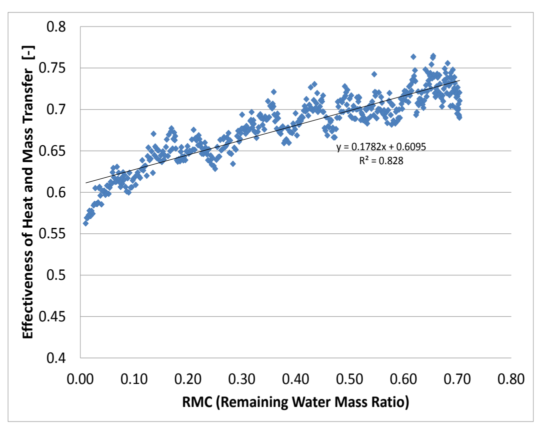

Figure 31. Heat and mass effectiveness of first generation drum.

Figure 32 shows the compressor isentropic efficiency as a function of the pressure ratio. It should be mentioned that the new rotary compressor is a low-cost option but is less efficient than the previous Tecumseh compressor, having average isentropic efficiency 55% versus 63%. For modeling the compressor, we assumed a constant isentropic efficiency of 55% and volumetric efficiency of 90% with a displacement volume of 12.2 cm^3 (0.7445 in^3).

The compressor shell heat loss ratio is defined as the amount of heat lost from, and stored in, the compressor shell divided by the electrical consumption of the compressor. Figure 33 depicts the compressor shell-heat loss ratio relative to the compressor power as a function of the compressor discharge saturation temperature to account for the energy balance across the compressor. The compressor's metal parts tend to reserve more heat at the startup at low-saturation temperature, and thus, the shell-heat loss ratio is larger at the beginning. It reached to 10% shell loss when the system approached to the final state of a drying process. This new compressor has less heat loss than the previous compressor, i.e., 10% versus 30% heat loss when reaching the final state because it is smaller in size. Arguably the heat loss should be correlated with compressor run time. This could be readily implemented in future work if desired.

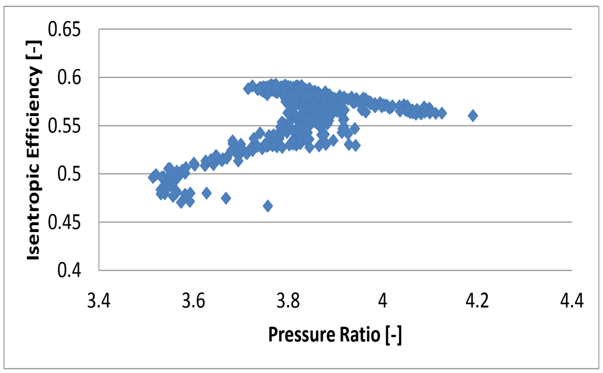

Figure 32. Compressor isentropic efficiency.

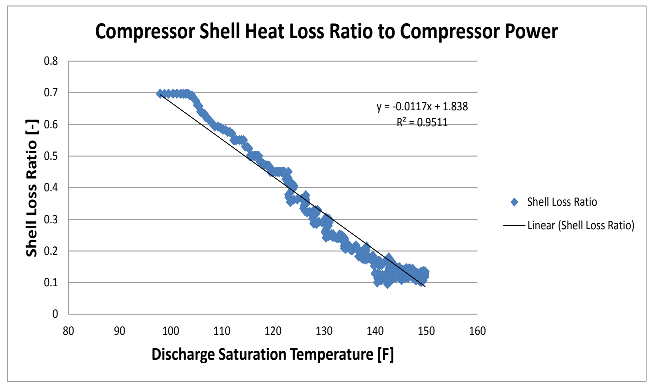

Figure 33. Compressor shell-heat loss ratio to compressor power.

This report aims to correlate the effect of air-side leakages in the system modeling and calibration. We use a duct blaster testing method and quantify the leakages in terms of C_v, as described in Figure 34).

From Duct Blaster get
Q [cfm] = $C\ \Delta P^n$

Convert Q to inches w.c.

Compute new C_v by forcing n = 0.5 and fitting data.

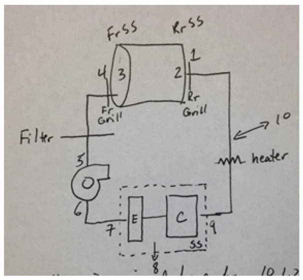

Description		As-received	Post-improvement
		C_v	
Rr Grill (Rear Duct to Drum Transition)	1	1.48	1.04
Rr. SS	2	14.47	14.47
Fr. SS	3	5.38	5.38
Fr Grill (Drum to Exit Duct Transition)	4	4.69	2.20
Exit Duct to Blower	5	0.25	0.25
Blower To Evap Duct	6	22.26	12.13
Evap Duct to HX	7	13.87	6.19
HX Misc	8	18.38	18.38
HX to Rear Duct	9	3.44	1.13
Rear Duct Misc	10	24.5	1.94
Misc between Rr Grill and Evap Duct Entrance	Mostly 4,5	38.10	28.14
Total Calculated Cv		146.87	91.30
Total Measured Cv		159.08	98.38
		Leakage Area (in^2)	
LBL ELA (in^2)		~3.3	1.4

Figure 34. Leakage measurements at multiple locations.

Figure 35 illustrates the measured local static pressures [in W.C.] and the resultant leaked airflow rates [CFM]. The major leakages which have sensible impacts on the system performance, include leaking out from the blower to evaporator (Blower→Evap), 7 CFM; evaporator to condenser (Evap→Cond), 3 CFM; and leaking in from the rear grill to the drum (RrGrill→RrSS), 10 CFM. The leakages at the other locations were either small or had no impact on the heat and mass transfer process and can be ignored.

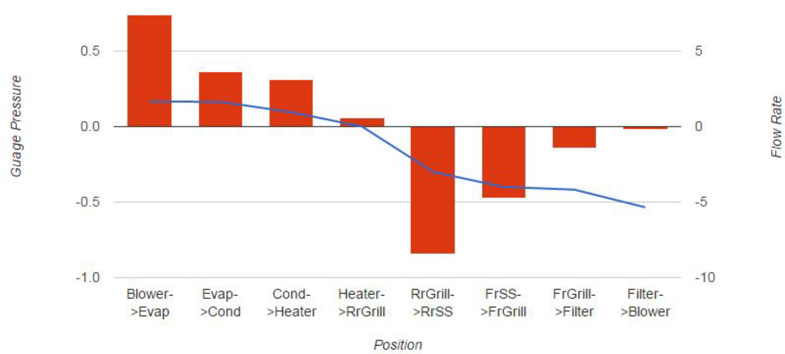

Figure 35. Local static pressures and leakage flow rates.

Using the inputs as above, we set up the HPCD system model and calibrated the air-side heat transfer multipliers of the evaporator and condenser to match near-steady-state suction and discharge pressures. Based on the calibrated system model, we were able to predict the transient clothes drying process. As shown in Figure 36 and Figure 37, the predicted suction and discharge pressure match the measurements in both the numbers and trends, respectively.

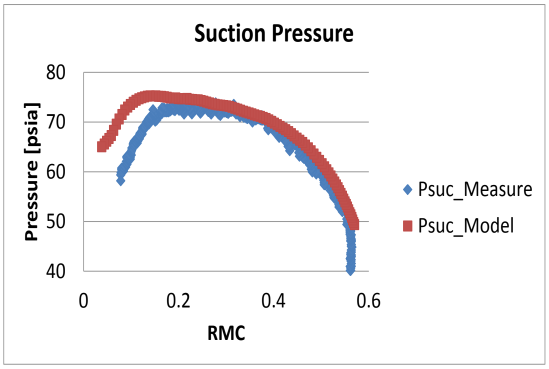

Figure 36. Measured and predicted suction pressures.

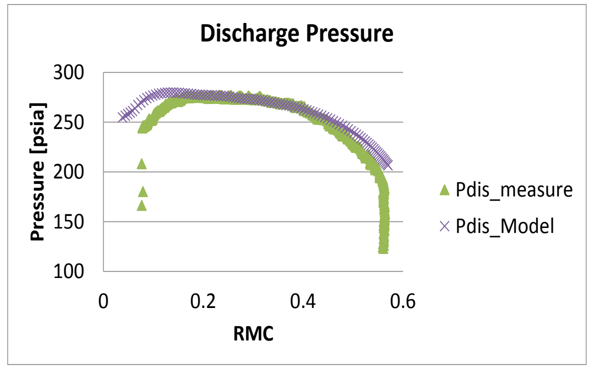

Figure 37. Measured and predicted discharge pressures.

As a result of the accurate refrigerant-state point predictions, the model predicted the compressor power consumption fairly accurately, as indicated in Figure 38.

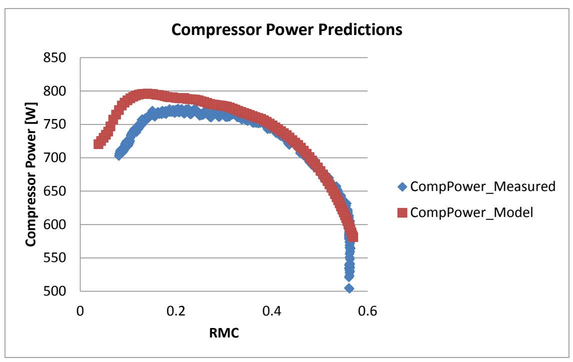

Figure 38. Measured and predicted compressor powers.

Figure 39 to Figure 41 show comparisons of predicted and measured air-state points across the heat pump system, i.e., evaporator inlet air temperature and humidity and condenser outlet air temperature. The results demonstrate that the HPCD design model achieved model validation of 2 K or better for key psychrometric state point temperatures and 5% or better for humidity ratios.

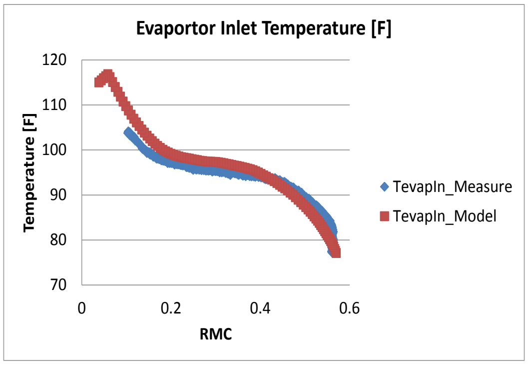

Figure 39. Measured and predicted evaporator inlet air temperatures.

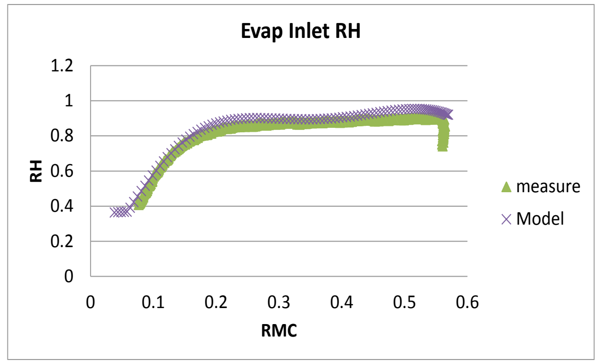

Figure 40. Measured and predicted evaporator inlet air relative humidities.

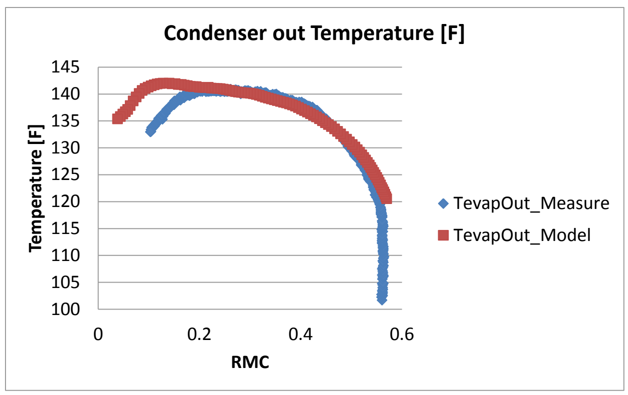

Figure 41. Measured and predicted condenser exit air temperatures.

To validate the robustness of the calibrated model, we extend the predictions for an extreme case which ran an electric booster heater for the first 10 minutes of the process, using the same set of calibration factors. Figure 42 to Figure 44 present the refrigerant pressures and compressor power predictions when running the electric heater for the first 10 minutes. It should be mentioned that the peaks in the figures occurred at the moment the heater was turned off. Without additional calibrations, the HPCD still captured the trends perfectly. It means that our design model is able to simulate the true physics.

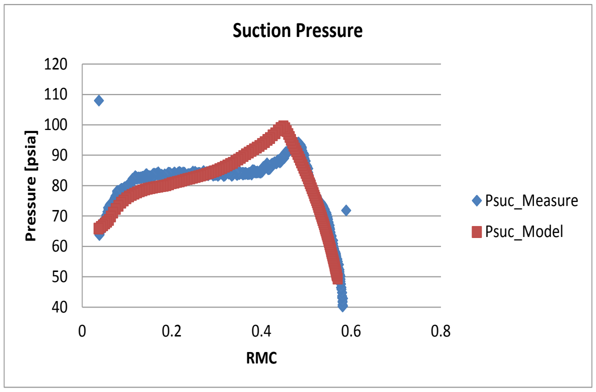

Figure 42. Measured and predicted suction pressures with running heater for 10 minutes.

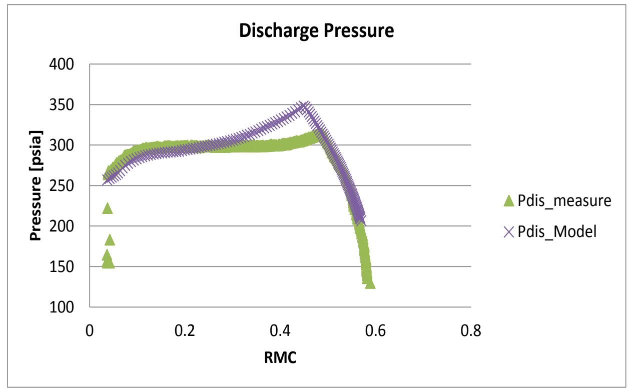

Figure 43. Measured and predicted discharge pressures with running heater for 10 minutes.

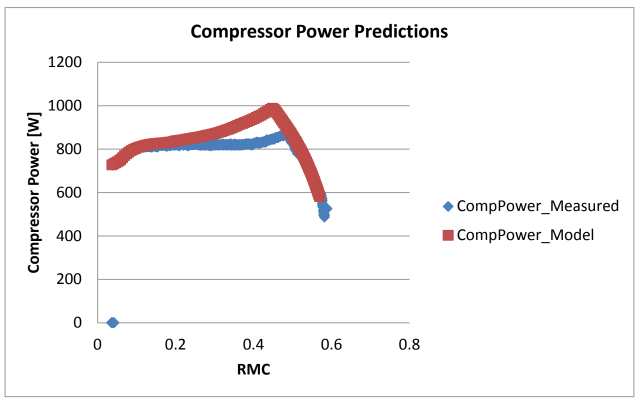

Figure 44. Measured and predicted compressor powers with running heater for 10 minutes.

ORNL conducted a matrix of HPCD experiments in which the time the heater was on, charge mass (average subcooling degree), and superheat degree (opening of the throttling device) varied, as was shown in Table 5. Table 17 below shows additional parameters relevant to the vapor compression model including the measured maximum compressor discharge temperature.

Table 17. Test matrix of varying the time the heater was on, charge mass, and superheat degree

	Average Condenser Exit Subcooling [°R]	Average Evaporator Exit Superheat [°R]	Heater On Time [min]	Energy Factor	Cycle Time [min]	Max Discharge T [°F]
1	12.6	7.7	0	6.684	71.4	184
2	13.2	19.5	0	6.625	72.7	198
3	11.0	7.6	10	5.946	62.7	186
4	11.3	19.3	10	6.095	62.1	195
5	28.1	7.9	0	6.109	72.9	193
6	25.7	20.1	0	6.141	74.3	203
7	17.6	8.3	10	5.499	64.1	191
8	18.0	20.4	10	5.602	64.2	202
9	21.9	8.6	0	6.356	71.1	191
10	22.7	19.7	0	6.306	74.6	200
11	17.3	8.8	10	5.781	63.2	191
12	18.6	19.8	10	5.825	61.9	203

We ran the calibrated HPCD model to simulate the test matrix. Table 18 presents the prediction deviations. Dev_EF is the relative deviations between the predicted and measured energy factors. Dev_Time presents absolute differences in the cycle time. Dev_DiscT indicates absolute differences of the compressor discharge temperature. We see the model can predict the energy factors within 10%, with the maximum deviation occurring at the extreme subcooling degree, i.e., overcharged. The cycle run time can be predicted within 5 minutes. The predicted discharge temperatures are acceptable due to the inherent uncertainty in the measurement arising from the difference between the refrigerant side temperature and the tube surface measurement.

Table 18. Prediction deviations of the test matrix

	Dev_EF	Dev_Time [min]	Dev_DiscT [°F]
1	-4.0%	-0.1	7.8
2	-2.5%	-0.7	2.7
3	-3.9%	1.1	19.4
4	-5.2%	2.1	17.7
5	9.2%	-4.5	1.5
6	10.0%	-5.3	0.4
7	6.9%	-1.6	13.6
8	2.5%	-1.8	21.3
9	1.1%	-1.1	7.2
10	3.6%	-4.5	5.9
11	-0.9%	-0.4	20.5
12	0.3%	0.7	15.3
Average	1.4%	-1.3	11.1
Stdev	4.9%	2.2	7.4
Max dev	10.0%	5.3	21.3

3.6.5 Model-Based Optimization

In order to identify the best combination of airflow rate and condenser subcooling degree (system charge), we ran a parametric study to simulate the EF as a function of the airflow rate in CFM and subcooling degree, as shown in the contour plot in Figure 45.

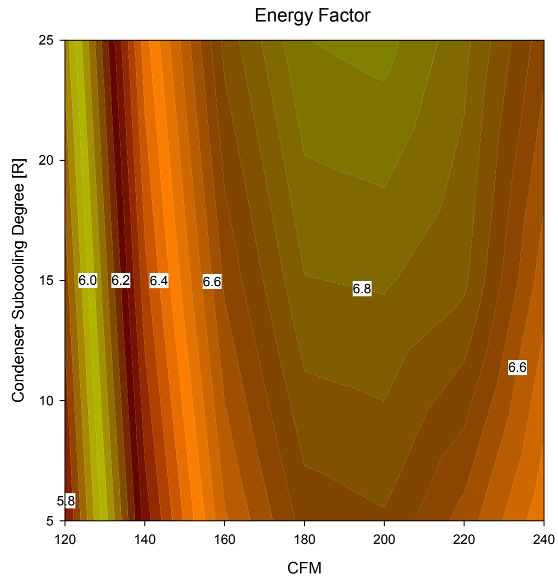

Figure 45. EF changing with airflow rate and condenser subcooling degree.

When varying the airflow rate, it was assumed that fan power = coefficient * CFM^3, where the coefficient obtained from the baseline blower at 120 CFM. As shown in Figure 45, the airflow rate has a major impact on the EF, with the optimum at around 180 CFM. The condenser subcooling degree has a secondary impact. Increasing the system charge elevates the condensing temperature and air temperature out of the condenser and boosts the evaporator cooling capacity. This adds more heat to the closed system and accelerates the drying process. However, higher charge leads larger compressor power consumption. There is a trade-off in adding the system charge. In addition, higher system charge tends to trip the compressor quicker.

We ran a parametric study to identify optimum leak points, which include

- three leak-outs: LEAKFANOUT (after fan), LEAKEVAPOUT (after evaporator), LEAKCONDOUT (after condenser)
- two leak-ins: LEAKDOWNIN (leak in downstream the drum), and leak in upstream the drum.

We simulated three total leaked flow rates, 10 CFM total, 20 CFM total, 40 CFM total.

- Three leak-out ratios: 10%, 50%, and 90% of the total leaked rate for each of the three leak-out points
- Three leak-in ratios: 10%, 50% and 90% for the downstream-drum leak-in.

In Table 19, the Max EF of each total leaked flow rate is highlighted in yellow. They all uniformly point to Max leak-out after fan and Max leak-in upstream of the drum (i.e., min leak in downstream of the drum). Table 19 gives the detailed simulation matrix.

Table 19. Parametric simulation of multi-point leakages

	LEAKFANOUT	LEAKEVAPOUT	LEAKCONDOUT	LEAKINDOWNIN	EF	DryTime
	[ft^3/hr]	[ft^3/hr]	[ft^3/hr]	[lbm/hr]		[min]
total leak: 10 CFM	540	30	30	39.8844	6.42	69.75
	300	150	150	39.8844	6.45	69.15
	60	270	270	39.8844	6.37	69.68
	30	540	30	39.8844	6.36	69.04
	150	300	150	39.8844	6.38	69.53
	270	60	270	39.8844	6.42	69.71
	30	30	540	39.8844	6.49	69.02
	150	150	300	39.8844	6.43	69.36
	270	270	60	39.8844	6.38	69.57
	540	30	30	22.158	6.46	69.24
	300	150	150	22.158	6.47	68.78
	60	270	270	22.158	6.49	68.39
	30	540	30	22.158	6.39	68.76
	150	300	150	22.158	6.39	69.30
	270	60	270	22.158	6.46	69.22
	30	30	540	22.158	6.45	69.41
	150	150	300	22.158	6.47	68.91
	270	270	60	22.158	6.48	68.46
	540	30	30	4.4316	6.50	68.66
	300	150	150	4.4316	6.52	68.18
	60	270	270	4.4316	6.46	68.56
	30	540	30	4.4316	6.44	68.05
	150	300	150	4.4316	6.46	68.49
	270	60	270	4.4316	6.50	68.67
	30	30	540	4.4316	6.49	68.90
	150	150	300	4.4316	6.52	68.21
	270	270	60	4.4316	6.46	68.50
total leak: 20 CFM	1080	60	60	79.7688	6.54	70.26
	600	300	300	79.7688	6.49	70.32
	120	540	540	79.7688	6.52	69.48
	60	1080	60	79.7688	6.45	68.98
	300	600	300	79.7688	6.45	70.13
	540	120	540	79.7688	6.55	70.10
	60	60	1080	79.7688	6.53	70.48
	300	300	600	79.7688	6.48	70.39
	540	540	120	79.7688	6.44	70.32
	1080	60	60	44.316	6.55	70.11
	600	300	300	44.316	6.59	69.15
	120	540	540	44.316	6.53	69.23
	60	1080	60	44.316	6.45	68.74

Table 19. Parametric simulation of multi-point leakages (continued)

	LEAKFANOUT	LEAKEVAPOUT	LEAKCONDOUT	LEAKINDOWNIN	EF	DryTime
	[ft^3/hr]	[ft^3/hr]	[ft^3/hr]	[lbm/hr]		[min]
	300	600	300	44.316	6.54	68.89
	540	120	540	44.316	6.56	69.93
	60	60	1080	44.316	6.65	69.24
	300	300	600	44.316	6.59	69.21
	540	540	120	44.316	6.53	69.13
	1080	60	60	8.8632	6.68	68.65
	600	300	300	8.8632	6.62	68.75
	120	540	540	8.8632	6.65	67.89
	60	1080	60	8.8632	6.55	67.64
	300	600	300	8.8632	6.56	68.60
	540	120	540	8.8632	6.69	68.51
	60	60	1080	8.8632	6.68	68.80
	300	300	600	8.8632	6.62	68.80
	540	540	120	8.8632	6.56	68.81
total leak: 40 CFM	2160	120	120	159.5376	6.47	73.00
	1200	600	600	159.5376	6.44	72.06
	240	1080	1080	159.5376	6.41	71.20
	120	2160	120	159.5376	6.27	70.46
	600	1200	600	159.5376	6.33	71.73
	1080	240	1080	159.5376	6.48	72.56
	120	120	2160	159.5376	6.45	73.22
	600	600	1200	159.5376	6.43	72.15
	1080	1080	240	159.5376	6.42	71.06
	2160	120	120	88.632	6.61	71.28
	1200	600	600	88.632	6.54	70.83
	240	1080	1080	88.632	6.57	69.34
	120	2160	120	88.632	6.48	67.96
	600	1200	600	88.632	6.48	69.96
	1080	240	1080	88.632	6.61	71.00
	120	120	2160	88.632	6.60	71.47
	600	600	1200	88.632	6.54	70.89
	1080	1080	240	88.632	6.57	69.24
	2160	120	120	17.7264	6.84	68.77
	1200	600	600	17.7264	6.73	68.67
	240	1080	1080	17.7264	6.74	67.44
	120	2160	120	17.7264	6.57	66.85
	600	1200	600	17.7264	6.64	68.12
	1080	240	1080	17.7264	6.84	68.52
	120	120	2160	17.7264	6.84	68.87
	600	600	1200	17.7264	6.73	68.71
	1080	1080	240	17.7264	6.74	67.36

3.7 EES HPCD SYSTEM MODEL

A simplified version of the model was implemented in Engineering Equation Solver (EES). The next two figures show the state points used in this model.

First, Figure 46 shows the psychrometric state points with the three thermodynamic (refrigeration cycle) state points with which they interacted in the model. Figure 47 shows the refrigeration cycle state points. Figure 48 shows more detail about the assumption for the interaction between the psychrometric (air) and thermodynamic (refrigeration cycle) state points, based on assumption of fixed approach temperatures.

Note that the right side diagram in Figure 46 has one extra air state point due to the inclusion of a heater. The modeling discussed in this section did not employ the heater.

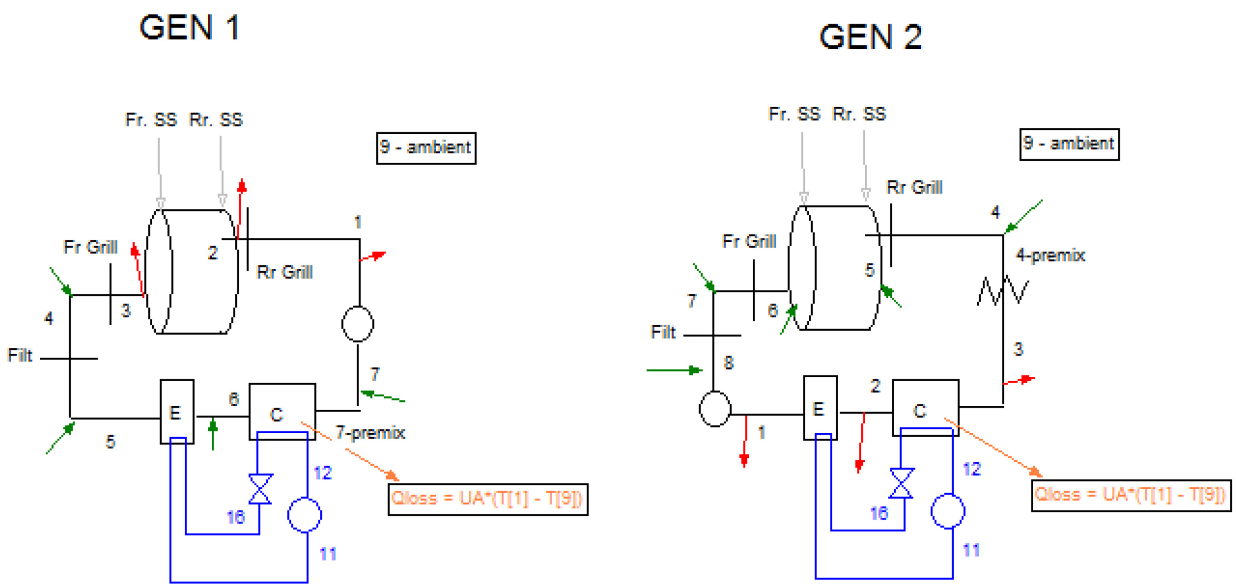

Figure 46. First generation (pressurized drum) and second generation (negative pressure drum) state points in EES model. Note SS = sliding seal.

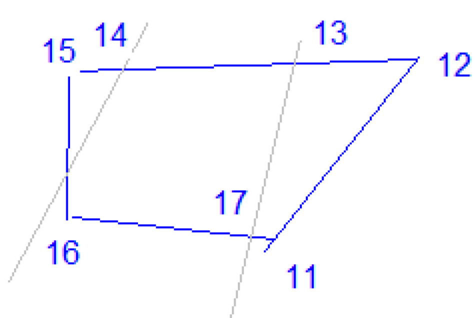

Figure 47. Thermodynamic (refrigeration cycle) state points used in EES model.

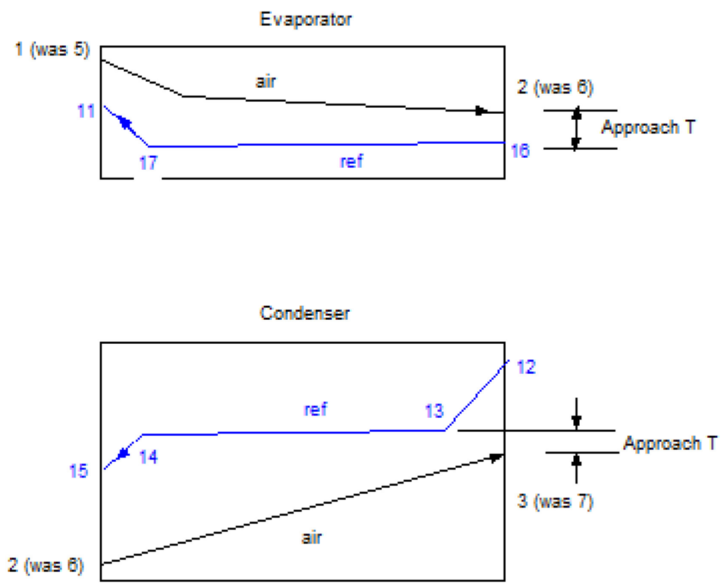

Figure 48. Definition of fixed approach temperatures used in EES model. Refrigerant state points are shown in blue, and psychrometric state points in black, with first and second generation designations shown.

Compared to the HPDM VC model, the EES thermodynamic model was much less sophisticated with regard to the VC cycle model. It contained independent calculations of efficiency (COP) and capacity.

The COP was calculated as being 35% of the Carnot efficiency, where Carnot is computed based on T17 (the suction saturation temperature) and T13 (the discharge saturation temperature).

To calculate the heat pump evaporator capacity, it was assumed that the compressor ran at fixed speed with constant volumetric efficiency, and that the evaporator capacity was proportional to refrigerant mass flow rate. The refrigerant mass flow rate (and thus evaporator cooling capacity) was calculated as being proportional to the compressor superheated suction density. At a reference density of 31.42 kg/m^3 (corresponding to R134a at 665.8 kPa and 30°C, i.e., a saturation temperature of 25°C with 5 K superheat), the capacity was calibrated to 1.58 kW (and higher capacities at high suction densities).

The psychrometric state points were solved based on an overall mass balance and individual equations for flow coefficient at each segment. An example solution is shown in Table 20. Depending on pressurization (positive or negative) and the presence or absence of heat transfer (diabatic or adiabatic), each state point used one of four cases (and the drum was a special fifth case):

1. <u>adiabatic, positive pressure case</u>: set T and w equal to previous segment

2. <u>diabatic, positive pressure case</u>: set w equal to previous segment and solve for $T = f(w, h)$ where enthalpy is derived from an energy balance

3. <u>adiabatic, negative pressure case</u>: solve for h and w by solving energy balance and species balance for mixing of air at previous state point with ambient air, in the proportion dictated by the leakage rate from the pneumatic solver

4. diabatic, negative pressure case: first, solve for h_{premix} by energy balance based on diabatic heat exchange. Then use h_{premix} as the input to the calculation used in the adiabatic, negative pressure case

5. drum: special case, where process is isenthalpic and effectiveness of heat and mass transfer is used to calculate temperature and humidity changes

The following experimentally measured values were used directly as inputs to the model:

- drum outlet relative humidity (88%)
- evaporator outlet humidity (95%)
- Measured CFM at blower
- Measured pressure drops across each component

Regarding the component pressure drops, it is important to distinguish this from the pressures relative to ambient. The pressures relative to ambient were computed by the model, while the pressure drops of each component were input to the model.

Table 20. Sample state point outputs for EES model of second generation prototype

Sort	1 T_i	2 RH_i	3 h_i	4 w_i	5 CvL_i	6 $CFML_i$	7 ρ_i	8 $rho2_i$	9 mL_i	10 $\dot{m}_{da,i}$	11 $\dot{V}_{da,i}$	12 $P_{gage,i}$	13 DP_i	14 P_i	15 $index_i$	16 $h_{premix,i}$	17 $w_{premix,i}$
[1]	31.95	0.8706	99.76	0.02643	2	1.631	1.139		0.0008767	0.09678	0.08495	0.6648	0.03	0	1		
[2]	26.76	0.95	80.99	0.02121	14.5	11.55	1.162		0.006337	0.09044		0.6348	0.37	-0.03	2		
[3]	48.62	0.2899	103.8	0.02121	16.5	8.49	1.09	1.083	0.004368	0.08607		0.2648	0.27	-0.4	3		
[4]	48.62	0.2899	103.8	0.02121	34.8	-2.513	1.09	1.083	-0.001293	0.08736		-0.005214	0.01	-0.67	4		
[5]	48.29	0.2926	103.1	0.02105	19.2	-2.368	1.085		-0.001212	0.08858		-0.01521	0.09	-0.68	5	103.8	0.02121
[6]	32.44	0.88	103.1	0.02752	18.6	-6.033	1.137		-0.003237	0.09181		-0.1052	0.56	-0.77	6		
[7]	32.27	0.8769	101.9	0.02715	4.3	-3.507	1.137		-0.001883	0.0937		-0.6652	0.66	-1.33	7	103.1	0.02752
[8]	31.95	0.8706	99.76	0.02643	6.3	-7.252	1.139		-0.003899	0.09759		-1.325		-1.99	8	101.9	0.02715
[9]	23.89	0.5	47.5	0.009236													
[10]																	
[11]	24.76						36.15										
[12]																	
[13]	55.62																
[14]																	
[15]																	
[16]																	
[17]	19.76																

Figure 49 shows the calibration of the model against a single UEF evaluation. The model was calibrated by tuning three parameters as follows:

1. the *nominal evaporator capacity* ($Q_{evap,nom}$ = 1.55 kW), which determines evaporator cooling capacity as proportional to compressor suction density, was tuned so that T[2] (evaporator air outlet temperature) matched the experimental value in the baseline experimental case.

2. the *composite heat loss coefficient* (UA_{loss} = 0.01689), which determines the convective heat losses due to compressor shell and miscellaneous losses, was tuned so that T[4] (drum entering air temperature) matched the experimental value in the baseline trial.

a. This Q_{loss} was subtracted from the air enthalpy at constant absolute humidity between the condenser and drum, and was proportional to the temperature difference between hottest air temperature and ambient air temperature according to $Q_{loss} = UA_{loss}$*(T[4] – T[9]).

b. Although leakage-related heat losses are captured directly by the model, this UAloss term was needed to account for compressor shell losses, conduction/radiation losses from various surfaces, and transient heat-storage losses.

c. The leakage-related losses plus the UA_{loss} composite losses will equal the total difference between condenser and evaporator capacity. At a typical T[4] of 49°C, the value of Q_{loss} was typically around 380 W (or ~60% of compressor work), with an additional 240 W (the other 40%) lost via leakage.

3. The *fraction of Carnot efficiency* of the vapor compression cycle ($f_{Ct} = 0.32$) was set so that the compressor work matched the experimental value for the baseline trial. Carnot COP was calculated at T[17] and T[13], the refrigerant evaporating and condensing temperatures (see Figure 47 and Figure 48). The cooling COP of the modeled cycle was computed as $COP_{clg} = f_{Ct}*COP_{Ct}$.

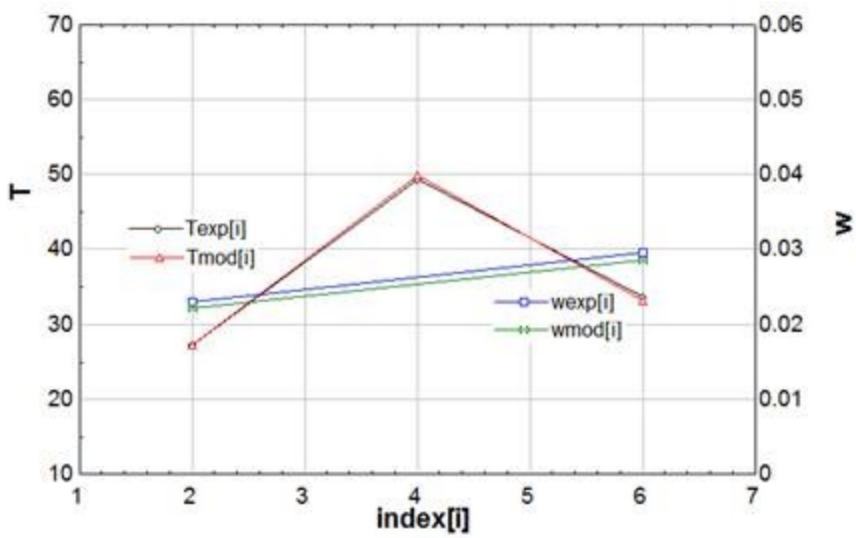

Figure 49. The EES model was calibrated to match three key state points (2, 4, and 6) against a single baseline experimental CEF trial

To validate this model a final test matrix was conducted in which artificial leaks were introduced and measured in the prototype ducting. The model was able to capture the changes in system performance, and introducing larger leakage areas between the blower and evaporator and at the rear grill had a slightly favorable outcome for efficiency and dry time.

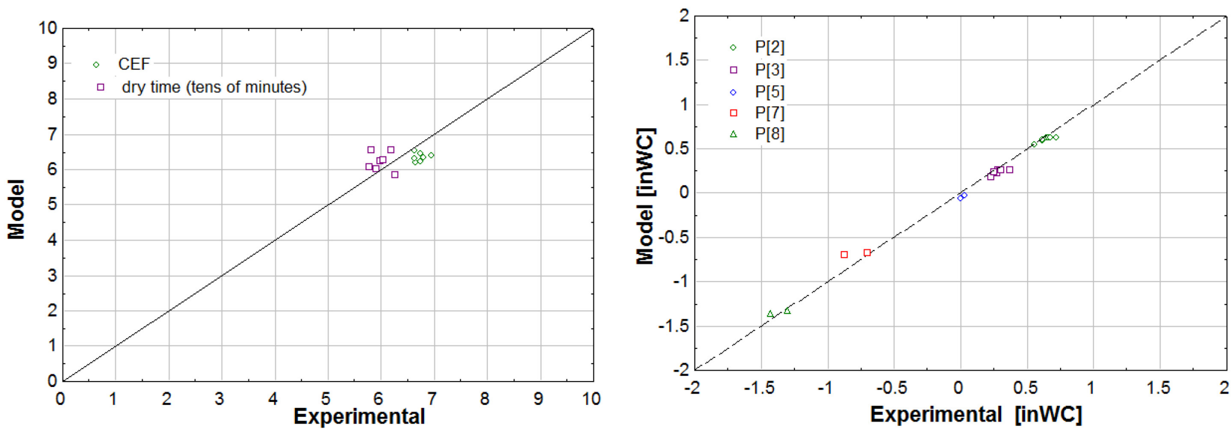

Figure 50. Experimental validation of HPCD system model CEF and dry time on left, and gauge pressures on right.

At the standard second generation conditions, assigning absolute uncertainties of one C_v point revealed that the sensitivities of each C_v were as shown below. The leakages just before the blower dominated. Further study of this diagram reveals the following:

- Higher leakage at state points 7 and 8 strongly adversely affects dry time and EF.
- Every leakage that is good for dry time is also good for EF.
- Three leakage locations have positive effect: state points 2, 4, and 6.
  - When dry time influence is normalized, if Cv_4 has 1 unit of influence, then Cv_2 has 8 and Cv_6 has 4.
  - When EF influence is normalized, if Cv_4 has 1 unit of influence, then Cv_2 has 3 and Cv_6 has 4.
- State points 4 and 6 decrease dry time by 1 minute for every 0.06 point increase in EF.
- State point 2 decreases dry time by 1 minute for every 0.02 point increase in EF.
- In other words, Cv_2 is the strongest way to decrease dry time, with a slightly positive effect on EF.

Variable±Uncertainty	Partial derivative	% of uncertainty
drytime = 56.94±2.851		
CvL_1 = 2±1	∂drytime/∂CvL_1 = 0.3828	1.80 %
CvL_2 = 14.5±1	∂drytime/∂CvL_2 = -0.3759	1.74 %
CvL_3 = 16.5±1	∂drytime/∂CvL_3 = 0.3379	1.40 %
CvL_4 = 34.8±1	∂drytime/∂CvL_4 = -0.04755	0.03 %
CvL_5 = 19.2±1	∂drytime/∂CvL_5 = 0.2736	0.92 %
CvL_6 = 18.6±1	∂drytime/∂CvL_6 = -0.2025	0.50 %
CvL_7 = 4.3±1	∂drytime/∂CvL_7 = 1.592	31.20 %
CvL_8 = 6.3±1	∂drytime/∂CvL_8 = 2.252	62.40 %
EF = 6.914±0.1405		
CvL_1 = 2±1	∂EF/∂CvL_1 = -0.02257	2.58 %
CvL_2 = 14.5±1	∂EF/∂CvL_2 = 0.007353	0.27 %
CvL_3 = 16.5±1	∂EF/∂CvL_3 = -0.01932	1.89 %
CvL_4 = 34.8±1	∂EF/∂CvL_4 = 0.002719	0.04 %
CvL_5 = 19.2±1	∂EF/∂CvL_5 = -0.01602	1.30 %
CvL_6 = 18.6±1	∂EF/∂CvL_6 = 0.01155	0.68 %
CvL_7 = 4.3±1	∂EF/∂CvL_7 = -0.07835	31.08 %
CvL_8 = 6.3±1	∂EF/∂CvL_8 = -0.1108	62.17 %

relative influence on	
dry time	EF
-0.170743	-0.204607
0.1674967	0.0668383
-0.150067	-0.17425
0.0211205	0.0245257
-0.121654	-0.144806
0.09004	0.104336
-0.707426	-0.707136
-1	-1

Figure 51. Uncertainty analysis of the Cv values using the EES model reveals their influences on cycle performance.

It should be noted that the results in Figure 51 are sensitive to all the details of the system, from the pressure drops to the leakage C_vs. In other words, the sensitivities are highly specific to a particular dryer. The effect of a change in a given C_v will depend on the value of parameters such as the other Cvs, component pressure drops, the selection of heat exchangers and compressor, and the drum effectiveness. More generalized conclusions have not been determined at this time. The state of the art has been advanced to introduce a fully coupled modeling methodology that will make such investigations possible.

3.8 HTML LEAKAGE MODEL

A simplified version of the leakage solver (described in Section 3.4.1) was developed in order to have a lightweight solver to investigate the impact of leakage. It was already introduced in a previous section, where Figure 12 shows the user interface and output of the model. The model used a javascript solver in order to iteratively determine the pressure and leakage solution for a user-defined set of leakage C_v coefficients and component pressure drops. The core of the solver is provided in Appendix A of this report.

3.9 COST ANALYSIS

Significant achievements were made by optimizing the compressor and heat exchangers and avoiding the need for active heat rejection componentry. Based on costing by GEA, the manufacturing cost premium relative to conventional dryers was reduced by half.

The cost reductions were achieved by selection of an appropriate low cost rotary compressor and pursuing model-based optimization of heat exchanger design. Although this sounds straightforward, the critical enabling factor was the design modeling framework developed in this project. The design model fully coupled the thermodynamic vapor compression model, psychrometric process model, effectiveness-based dryer drum model, and air leakage model. Due to the highly coupled nature of the heat pump dryer system, traditional rules of thumb for compressor selection and heat exchanger sizing are not suitable, and a sophisticated modeling approach delivered strong performance and cost benefits. The funding provided in this project allowed the team to pursue multiple generations of model development and prototype fabrication, enabling this new fully coupled integrated approach to heat pump clothes dryer design.

4. INVENTIONS AND COMMUNICATIONS

Inventions

Gluesenkamp, K.R.; Beers, David; Shen, Bo; Boudreaux, Philip. (2017). Design of heat pump clothes dryer for enhanced performance. ORNL Invention Disclosure 201703909, DOE S-138,567.

Communications

Journal Publications

Pradeep Bansal, Amar Mohabir, William Miller (2016). “A novel method to determine air leakage in heat pump clothes dryers.” *Energy* 96:1-7.

Conference Papers

Shen, B., Gluesenkamp, K., Bansal, P., Beers, D. (2016). “Heat pump clothes dryer model development.” *16th Refrigeration and Air Conditioning Conference*, Purdue University, West Lafayette, IN, 7/2016

Presentations and Other Communications

Gluesenkamp, K., Shen, B. (2017). “Heat Pump Clothes Dryer.” *2017 Building Technologies Office Peer Review*, Arlington, VA, March 13, 2017.

5. COMMERCIALIZATION POSSIBILITIES

As a result of the research conducted under this Cooperative Research and Development Agreement (CRADA), commercialization prospects are under consideration by the industry partner.

In addition, the dryer leakage evaluation techniques and the clothes dryer modeling tools developed in this project are both published in the academic literature and can provide opportunities for cost reduction and performance improvements by industry and researchers.

Finally, the cost reductions achieved in the research conducted under this CRADA greatly enhance the prospects for commercialization of heat pump clothes dryers in the United States.

6. REFERENCES

Ally, M.R.; B. Shen, 2010. “Direct Evaporative Precooling Model and Analysis”, ORNL Report ORNL/TM-2010/231. Available: http://info.ornl.gov/sites/publications/Files/Pub26605.pdf

ANSI/AHRI Standard 540-99, 2010. "Positive Displacement Refrigerant Compressors and Compressor Units," Air Conditioning and Refrigeration Institute, Arlington, VA.

Bansal, Pradeep, Amar Mohabir, and William Miller, 2016. "A novel method to determine air leakage in heat pump clothes dryers." *Energy*, 96, issue C, pp. 1–7.

Braun, J.E., S.A. Klein, and J.W. Mitchell, 1989. "Effectiveness models for cooling towers and cooling coils", *ASHRAE Transactions*, Vol. 95, Pt. 2, pp. 164–174.

Dabiri, A.E. and C.K. Rice, 1981. "A Compressor Simulation Model with Corrections for the Level of Suction Gas Superheat," *ASHRAE Transactions*, Vol. 87, Part 2, pp.771–782.

Denkenberger, D., C. Calwell, N. Beck, B. Trimboli, D. Driscoll, and C. Wold, 2013. "Analysis of Potential Energy Savings from Heat Pump Clothes Dryers in North America," Ecova, CLASP and SEDI, Spokane.

Department of Energy, 2016. *Building Technologies Office Multi-Year Program Plan, Fiscal years 2016-2020.* February 2016. Available: https://energy.gov/sites/prod/files/2016/02/f29/BTO%20Multi-Year%20Program%20Plan%20-%20Final.pdf

Gluesenkamp, K., 2014. *Residential clothes dryer performance under timed and automatic termination test procedures*. ORNL publication 2014/431. Available at http://web.ornl.gov/sci/buildings/docs/2014-10-09-ORNL-DryerFinalReport-TM-2014-431.pdf

Ling, Jiazhen, and Hwang Yunho, 2013. *Two-stage heat pump clothes dryer*, CEEE Report, University of Maryland.

Rice, C.K., 1997. "DOE/ORNL Heat Pump Design Model, Overview and Application to R-22 Alternatives," 3rd International Conference on Heat Pumps in Cold Climates, Wolfville, Nova Scotia, Canada, Aug. 11–12, 1997; Caneta Research, Inc., Mississauga, Ontario, Canada, November, pp.43–66.

Shen, B. and C.K. Rice, 2014. HVAC System Optimization with a Component Based System Model – New Version of ORNL Heat Pump Design Model, Purdue HVAC/R Optimization short course, International Compressor & refrigeration conferences at Purdue, Lafayette, USA, 2014; web link: http://hpdmflex.ornl.gov/hpdm/wizard/welcome.php

US Code of Federal Regulations, 2015. Title 10: "Energy;" Part 430, "Energy Conservation Program for Consumer Products;" Subpart B, "Test Procedures;" Appendix D1, "Uniform Test Method for Measuring the Energy Consumption of Clothes Dryers." 10 CFR 430.

Wetter, M., 2009. *GenOpt® Generic Optimization Program User Manual Version 3.0.0*, Lawrence Berkeley National Laboratory Technical Report LBNL-2077E.

APPENDIX A. HTML/JAVASCRIPT-BASED LEAKAGE SOLVER

```
<!-- saved from
url=(0142)file:///C:/Users/pxy/AppData/Local/Microsoft/Windows/Temporary%20Internet%20Files/Content.Outlook/OPLV27QG/DLCalculator_blower_after_drum.html -->
<html xmlns="http://www.w3.org/1999/xhtml"><head><meta http-equiv="Content-Type"
content="text/html; charset=windows-1252"><script type="text/javascript"
src="./DLCalculator_blower_after_drum test_matrix PRB_files/loader.js.download"></script>
<script type="text/javascript" src="./DLCalculator_blower_after_drum test_matrix
PRB_files/loader.js(1).download"></script><script type="text/javascript">
var dp = new Array(8).fill(0);//pressure drop in the section, read from input
var dp0 = new Array(8).fill(0);//pressure difference from the first section, calculate from dp
var pabs = new Array(8).fill(0);//gauge pressures, calculate from resulting p0 and dp0
var CvL = new Array(8).fill(0);//leak coefficient, read from input
var cfmL = new Array(8).fill(0);//leakage, calculate from guessing p0 and dp0 and CvL
var iter = 0, residual = 0, totalDp = 0;
function updateParameters(){
dp[1] = Number(document.getElementById('DP1Text').value);
dp[2] = Number(document.getElementById('DP2Text').value);
dp[3] = Number(document.getElementById('DP3Text').value);
dp[4] = Number(document.getElementById('DP4Text').value);
dp[5] = Number(document.getElementById('DP5Text').value);
dp[6] = Number(document.getElementById('DP6Text').value);
dp[7] = Number(document.getElementById('DP7Text').value);
CvL[0] = Number(document.getElementById('Leak0Text').value);
CvL[1] = Number(document.getElementById('Leak1Text').value);
CvL[2] = Number(document.getElementById('Leak2Text').value);
CvL[3] = Number(document.getElementById('Leak3Text').value);
CvL[4] = Number(document.getElementById('Leak4Text').value);
CvL[5] = Number(document.getElementById('Leak5Text').value);
CvL[6] = Number(document.getElementById('Leak6Text').value);
CvL[7] = Number(document.getElementById('Leak7Text').value);

totalDp = 0;
for(i = 0; i < 8; i++){
totalDp += dp[i];
if(i>0){
dp0[i]=dp0[i-1]+dp[i];
}
}
}
function massBalance(p1){
```

```
var p_local;
var massResidual = 0;
for(i = 0; i < 8; i++){
p_local = p1 - dp0[i];
cfmL[i] = Math.sign(p_local)*CvL[i]*Math.sqrt(Math.abs(p_local));
massResidual += cfmL[i];
}
return massResidual;
}
function opt(p0,tolerance,maxIter,tau){
if(tolerance===undefined){
tolerance = 1e-5;
maxIter = 2000;
tau = 1e-4;
}
residual = 1;
iter = 0;
var p00 = p0;
for(i = 0; i < maxIter && Math.abs(residual)>tolerance; i++){
residual = massBalance(p00);
p00 -= tau * residual;
iter ++;
}
return p00;
}
function updateResults(){
for(i = 0; i < 8; i++){
pabs[i] = pabs[0]-dp0[i];
}
```